

Northumbria Research Link

Citation: Hosseini Biroun, Seyedmehdi, Rahmati, Mohammad, Tao, Ran, Torun, Hamdi, Jangi, Mehdi and Fu, Richard (2020) Dynamic Behavior of Droplet Impact on Inclined Surfaces with Acoustic Waves. *Langmuir*, 36 (34). pp. 10175-10186. ISSN 0743-7463

Published by: American Chemical Society

URL: <https://doi.org/10.1021/acs.langmuir.0c01628>
<<https://doi.org/10.1021/acs.langmuir.0c01628>>

This version was downloaded from Northumbria Research Link:
<http://nrl.northumbria.ac.uk/id/eprint/44259/>

Northumbria University has developed Northumbria Research Link (NRL) to enable users to access the University's research output. Copyright © and moral rights for items on NRL are retained by the individual author(s) and/or other copyright owners. Single copies of full items can be reproduced, displayed or performed, and given to third parties in any format or medium for personal research or study, educational, or not-for-profit purposes without prior permission or charge, provided the authors, title and full bibliographic details are given, as well as a hyperlink and/or URL to the original metadata page. The content must not be changed in any way. Full items must not be sold commercially in any format or medium without formal permission of the copyright holder. The full policy is available online: <http://nrl.northumbria.ac.uk/policies.html>

This document may differ from the final, published version of the research and has been made available online in accordance with publisher policies. To read and/or cite from the published version of the research, please visit the publisher's website (a subscription may be required.)

This document is confidential and is proprietary to the American Chemical Society and its authors. Do not copy or disclose without written permission. If you have received this item in error, notify the sender and delete all copies.

**Dynamic behavior of droplet impact on inclined surfaces
with acoustic waves**

Journal:	<i>Langmuir</i>
Manuscript ID	la-2020-016283.R1
Manuscript Type:	Article
Date Submitted by the Author:	15-Jul-2020
Complete List of Authors:	H. Biroun, Mehdi; Northumbria University, Rahmati, Mohammad; Northumbria University Tao, Ran; Northumbria University; Shenzhen University Torun, Hamdi; Northumbria University, Electrical Engineering Jangi, Mehdi; University of Birmingham Fu, Yongqing; Northumbria University Faculty of Engineering and Environment, Department of Physics and Electrical Engineering

SCHOLARONE™
Manuscripts

1
2
3
4
5
6
7
8
9
10
11
12
13
14
15
16
17
18
19
20
21
22
23
24
25
26
27
28
29
30
31
32
33
34
35
36
37
38
39
40
41
42
43
44
45
46
47
48
49
50
51
52
53
54
55
56
57
58
59
60

Dynamic behavior of droplet impact on inclined surfaces with acoustic waves

Mehdi H. Biroun¹, Mohammad Rahmati¹, Ran Tao^{1,2}, Hamdi Torun¹, Mehdi Jangi³, Yongqing Fu^{1,}*

1: Faculty of Engineering and Environment, Northumbria University, Newcastle upon Tyne, NE1 8ST,

UK

2: Shenzhen Key Laboratory of Advanced Thin Films and Applications, College of Physics and
Optoelectronic Engineering, Shenzhen University 518060, China

3: Department of Mechanical Engineering, University of Birmingham, Birmingham, B15 2TT, UK

1
2 ABSTRACT: Droplet's impact on arbitrary inclined surfaces is of great interest for applications such as
3
4 anti-freezing, self-cleaning, and anti-infection. Research has been focused on texturing the surfaces to
5
6 alter the contact time and rebounding angle upon droplet impact. In this paper, using propagating surface
7
8 acoustic waves (SAW) along the inclined surfaces, we present a novel technique to modify and control
9
10 key droplet impact parameters, such as impact regime, contact time, and rebounding direction. A high-
11
12 fidelity finite volume method was developed to explore the mechanisms of droplet impact on the inclined
13
14 surfaces assisted by SAWs. Numerical results revealed that applying SAWs modifies the energy budget
15
16 inside the liquid medium, leading to different impact behavior. We then systematically investigated the
17
18 effects of inclination angle, droplet impact velocity, SAW propagation direction and applied SAW
19
20 power on the impact dynamics, and showed that by using SAWs, droplet impact on the non-textured
21
22 hydrophobic and inclined surface is effectively changed from deposition to complete rebound.
23
24 Moreover, the maximum contact time reduction up to ~50% can be achieved, along with an alteration
25
26 of droplet spreading and movement along the inclined surfaces. Finally, we showed that the rebounding
27
28 angle along the inclined surface could be adjusted within a wide range.
29
30
31
32
33

34
35 KEYWORDS: Surface acoustic wave, droplet impact, inclined surface, contact time, finite volume
36
37 method
38
39

40 INTRODUCTION

41
42
43 Over the past decades, liquid droplet impact on solid surfaces, on either flat, inclined or complex-
44
45 shaped surfaces, has been extensively studied because of its significance in scientific understanding and
46
47 industrial applications, including anti-fogging ¹, anti-icing ²⁻⁴, inkjet printing ⁵⁻⁸, agriculture ^{9,10}, spray
48
49 cooling ^{11,12}, self-cleaning ¹³⁻¹⁵, anticorrosion ¹⁶⁻¹⁸, internal combustion engines ^{19,20}, optical devices, ²¹
50
51 anti-infection surfaces, ²² water collection systems, ^{23,24} and liquid material transportation and
52
53 distribution ^{25,26}.
54
55
56
57
58
59
60

1
2 After the droplet impact on solid surfaces (either horizontal or inclined surfaces) and in the absence
3
4 of splashing, the droplet spreads on the solid surface to a maximum spreading diameter, and then
5
6 depending on the surface and liquid physiochemical properties and impact velocity, the droplet can
7
8 retract or permanently remain spread on the surface ²⁷. The droplet impact is controlled by kinematic,
9
10 surface, and potential energies and viscous dissipation in the liquid medium ²⁸. When the solid surface
11
12 is hydrophobic, less energy is dissipated during the impact, and droplet detachment from the surface as
13
14 a jet can often be observed ²⁹. Experimental studies from Bayer and Megaridis have shown that the
15
16 wetting properties of the surface affect the contact line velocity, capillary waves on the liquid-gas
17
18 interface during the early stages of the impact, contact angle hysteresis and the impact regime of the
19
20 droplet ³⁰.

21
22
23
24
25 In the last two decades, the droplet impact dynamics on the inclined surfaces have been investigated
26
27 in detail, using high-speed photography and advanced numerical methods. For instance, Sikalo et al.
28
29 investigated the effects of surface roughness and liquid viscosity on the dynamics of the droplet impact
30
31 on inclined surfaces. They reported the observation of asymmetry in the front and back sides of the
32
33 droplet after the impact ³¹. A few studies have attempted to explain the main contributing parameters in
34
35 the droplet impact regime on the inclined surfaces. For example, Bird et al. reported that the tangential
36
37 velocity vector plays a major role in the droplet splash dynamics on inclined surfaces ³². Chiarot et al. ³³
38
39 and Zhang et al. ³⁴ showed that the rebounding regime of the high-velocity impact of continuous droplet
40
41 stream on inclined superhydrophobic surfaces is functions of droplet ejection rate and impact velocity.
42
43
44

45
46 Moreover, different key parameters affecting the suppression of droplet splash on inclined surfaces
47
48 were systematically investigated by Hao et al. ³⁵. Yeong et al. also investigated the correlation between
49
50 parameters of impact dynamics on inclined surfaces (such as contact time and impact regime) and Weber
51
52 number ($We = \rho_l U_0^2 D_0 / \gamma_{LV}$ in which ρ_l , U_0 , D_0 , and γ_{LV} are density, impact velocity, initial diameter, and
53
54 surface tension of the droplet correspondingly) ³⁶. Antonini et al. observed six different rebounding
55
56 regimes, according to We numbers and superhydrophobic conditions ³⁷. LeClear et al. observed the
57
58
59
60

1 transition from Cassie-Baxter impact to the Wenzel impact during the droplet impact on tilted
2 superhydrophobic surfaces³⁸. Wang et al. showed that by increasing the inclination angle or impact
3 velocity, there is a noticeable contact time reduction due to asymmetric spreading and retract of the
4 impacting droplet³⁹.
5
6
7
8
9

10 Inspired by nature, a few passive techniques have been developed and applied to reduce the droplet
11 contact time on superhydrophobic and inclined surfaces.⁴⁰⁻⁴² For instance, Regulagadda et al. proposed
12 texturing the substrate with a triangular ridge to realize droplet ski-jumping from the surface, thus
13 leading to a contact time reduction of ~65%. Zhang et al. reported a 10%-30% contact time reduction
14 by using substrates patterned with varied posts and coated with nanoparticles for oblique droplet impact
15
16
17
18
19
20
21
22
23
24
25
26
27
28
29
30
31
32
33
34
35
36
37
38
39
40
41
42
43
44
45
46
47
48
49
50
51
52
53
54
55
56
57
58
59
60

Recently, SAW-based microfluidics has found many applications in biochemical analysis, lab on a
chip,⁴⁴ DNA sequencing^{45,46}, disease diagnosis⁴⁷, and drug delivery systems⁴⁸. SAW is generated by
applying a radio frequency (RF) signal to interdigital transducers (IDTs), which are patterned on a
piezoelectric substrate such as LiNbO₃ and zinc oxide film on a solid substrate. The amplitude of the
SAW and wave frequency can be altered by changing the applied RF signal power and IDT design,
respectively. When liquid phase (i.e., droplet or confined liquid in a microchannel) is positioned on the
SAW propagating path, it attenuates and changes the mode of SAW to leaky SAW due to the discrepancy
between the sound velocities in the solid and liquid medium⁴⁹. The leakage of the acoustic
energy/pressure into the liquid medium is along the Rayleigh angle, θ_R given by⁵⁰:

$$\theta_R = \sin^{-1}\left(\frac{v_L}{v_S}\right) \quad (1)$$

1 where v_L and v_S are wave velocities of sound in liquid and solid, respectively. Depending on the energy
2 transferred inside the liquid, internal streaming, transportation, jetting, and nebulization of the droplet
3 can be generated^{51,52}. SAW-based microfluidics has the advantages of large input energy, simple device
4 structure, fast operation, compatibility with sensing applications, remote control compared to other
5 microfluidic mechanisms.
6
7
8
9
10
11
12

13
14 Previously, we reported that by applying traveling surface acoustic waves (SAWs) to a droplet during
15 its impingement on a flat surface, the contact time could be effectively reduced⁵³. Our results showed
16 that the transferred SAW energy into the liquid medium during the impingement can alter the internal
17 recirculation field of the droplet, which leads to a faster detachment of droplet from the surface.
18
19
20
21
22
23

24 In this work, we propose to use SAWs for the active control of droplet impact dynamics (including
25 impact regime, contact time, and rebounding angle) on inclined surfaces. By applying SAWs with
26 different propagation directions and powers on inclined surfaces, the impact regime of the droplet can
27 be effectively modified. Additionally, different impact parameters such as contact time, maximum
28 spreading diameter, and rebounding angle can be dramatically altered. We expect that by applying
29 upward SAW (USAW) or downward SAW (DSAW) and as a result of changing the energy budget
30 within the liquid medium, the motion of the droplet's leading and trailing edges (See Figure 1 for
31 definitions) would be altered. Consequently, impact characteristics parameters such as contact time
32 (which is defined as the time between impact moment, t_i , and detachment moment, t_f), maximum
33 spreading ($\beta_{Max} = L_{Max}/D_0$, where D_0 is the initial droplet diameter, and L_{Max} is the maximum spreading
34 width along the direction tangential to the surface), movement along the surface (δ is the distance
35 between the impact and detachment points), and rebound angle ($\theta_{Rebound}$, which is defined as the
36 angle between the surface normal vector and the line connecting the separation point to the droplet tip
37 at the separation moment in an anticlockwise direction) could be altered in a programmable and
38 controllable way. Definitions of all these parameters are illustrated in Figure 1.
39
40
41
42
43
44
45
46
47
48
49
50
51
52
53
54
55
56
57
58
59
60

1
2 To examine the effect of SAW on droplet impact, we propose three scenarios, e.g., droplet free impact
3 (FI), droplet impact in the presence of USAW, and DSAW on the inclined surface, as illustrated in
4 Figures 1(a-c). To study the transferred energy of the SAW to the liquid phase, we assume that a body
5 force, \mathbf{f}_{SAW} is generated by the SAWs, and applied to the droplet along the Rayleigh angle:
6
7
8
9

$$10 \quad \mathbf{f}_{SAW} = -\rho(1 + \alpha_1^2)^{\frac{3}{2}} A^2 \omega^2 k \cdot \exp(2[kx + \alpha_1 kz]) \quad (2)$$

11
12 where symbols in bold are used to indicate the vector and tensor variables. In this equation $\alpha_1 =$
13

14 $\sqrt{(v_S/v_L)^2 - 1}$ is attenuation coefficient, A is wave amplitude, ω is the angular frequency, and k is leaky
15
16
17
18
19 SAW wave number⁵⁴. x and z are the tangential and normal positions based on the origin of the
20
21
22 coordinate at the incidence point of the SAW and droplet on the device surface.
23
24
25
26
27
28
29
30
31
32
33
34
35
36
37
38
39
40
41
42
43
44
45
46
47
48
49
50
51
52
53
54
55
56
57
58
59
60

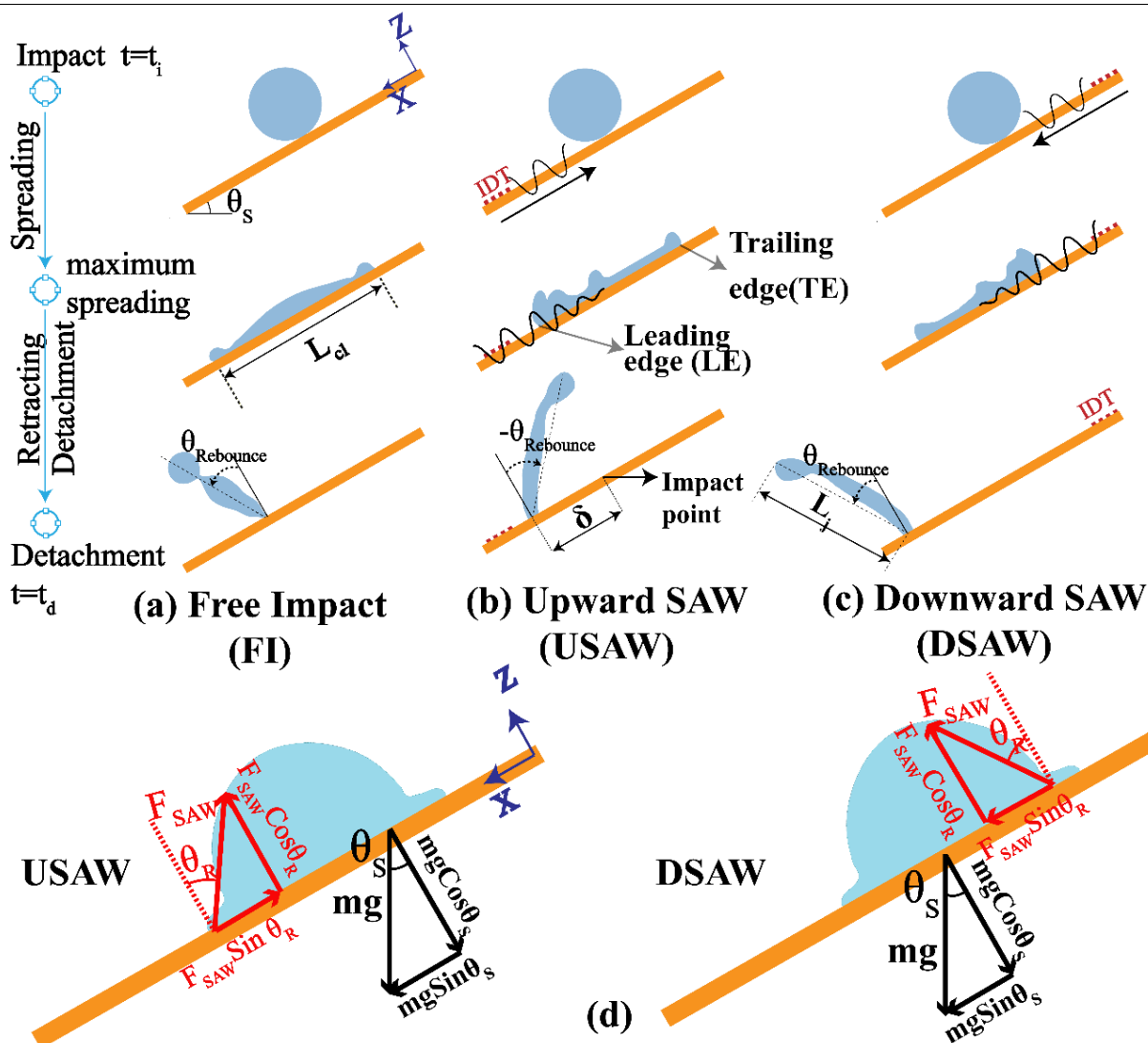


Figure 1. Schematic views of different scenarios of droplet impact on inclined surfaces. (a) Droplet free impact (FI), (b) Droplet impact in the presence of USAW, (c) Droplet impact in the presence of DSAW. The positive direction of the rebounding angle is in the anticlockwise direction from the surface normal direction. (d) Schematic view of SAW and gravitational force interaction.

By changing the surface inclination angle, SAW power and direction, the force balance between the tangential and normal components of applied SAW force and gravitational force are changed (see figure 1(d) and supplementary material S1). For the FI scenario, after the droplet impact on solid surfaces, the droplet spreads to a maximum spreading width and then retracts toward the center. During the droplet

1
2 impingement on the solid surface, two main forces along the surface resist against the liquid motion: 1)
3
4 A pinning force is generated along the three-phase contact line (TPCL) due to the contact angle
5
6 hysteresis and is a function of liquid surface tension, TPCL length, and receding and advancing contact
7
8 angles (e.g., $F_p = \frac{2\gamma_{LV}}{\pi} D(\cos \theta_{rec} - \cos \theta_{adv})$ where γ_{LV} is the surface tension coefficient, D is the
9
10 TPCL length, and θ_{rec} and θ_{adv} are the advancing and receding contact angles of the droplet on the
11
12 solid surface, respectively.^{55,56}). 2) The friction between the liquid and solid surface due to the shear
13
14 stress, which is a function of the viscosity of the liquid and the relative velocity between the fluid and
15
16 surface⁵⁷. If the initial energy of the droplet is high enough to overcome the energy dissipated by these
17
18 two forces and viscous dissipation within the liquid medium, the droplet can detach from the surface at
19
20 the end of the retract phase. The interaction between the resistive forces and the gravitational force would
21
22 be altered by applying the SAW force. Moreover, since SAW energy is applied to the liquid medium
23
24 during the impingement, the energy budget of the droplet can be effectively modified.
25
26
27
28
29

30 To investigate our hypotheses and reveal the complex physics behind the SAW effects on droplet
31
32 impact, we performed numerical simulations for the defined scenarios using a coupled level set volume
33
34 of fluid (CLSVOF) finite volume method. Afterward, we experimentally examined the droplet impact
35
36 dynamics in the presence of SAWs. To quantitatively compare the effect of SAW on the impact dynamics,
37
38 impact characteristics parameters such as contact time, maximum spreading width, droplet transition
39
40 along the surface, and rebound angle were analyzed as functions of SAW power and direction, surface
41
42 inclination angle and impact velocity.
43
44
45

46 Our results show that at a constant We number, by increasing the applied SAW power and regardless
47
48 of the SAW direction and surface inclination angle, the contact time of the impacting droplet can be
49
50 reduced. Additionally, the impact regime can be changed from deposition (in the FI scenarios) to a
51
52 complete rebound by applying SAW agitation. More interestingly, if the surface inclination angle is kept
53
54
55
56
57
58
59
60

1
2 a constant and the impact velocity (i.e., the We number) is altered, the impact regime at the lower We
3
4 numbers can be changed from deposition on the surface to complete rebound from the surface.
5
6
7

8 9 EXPERIMENTAL METHODS AND SAMPLE PREPARATION

10
11
12 **SAW Device Preparation.** Using a direct current magnetron sputter system (Nordiko Ltd.), a layer
13
14 of ZnO piezoelectric film with a thickness of $\sim 5.5 \mu\text{m}$ was deposited on Si substrates using a pure zinc
15
16 target (99.99%). The deposition parameters are as follows: a DC power of 400 W , an Ar/O₂ mass flow
17
18 ratio of 10/15 SCCM, and a chamber pressure of ~ 3.2 mTorr without any external substrate heating.
19
20 SAW devices were fabricated on ZnO film coated silicon wafer (see supplementary material Figure S3
21
22 for a scanning electron microscope (SEM) image of the film/substrate), on which two pairs of interdigital
23
24 transducers (IDT) were photolithographically patterned. The Cr/Au IDTs had the thicknesses of 20/100
25
26 nm and consisted of 30 pairs of fingers, with an aperture of 5 mm and different wavelengths of 64 to
27
28 200 μm . The resonant frequency of each SAW device was measured using an RF network analyzer
29
30 (HP8752A RF network analyzer). The SAW device surface was coated by a layer of CYTOP (Asahi
31
32 Glass Co.) with a thickness of ~ 200 nm. The droplet contact angle was measured to be $122^\circ \pm 2^\circ$ with a
33
34 contact angle hysteresis of $28^\circ \pm 6^\circ$. The RF signal was generated using a signal generator (Macroni2024)
35
36 and amplified with an RF amplifier (Amplifier research, 75A250) before being applied to the IDTs of
37
38 the SAW device. The applied power to the SAW IDTs was measured before each experiment using an
39
40 RF power meter (RACAL Equipment, 9104).
41
42
43
44
45

46
47 **Droplet Impact.** Droplets of deionized water with an initial diameter of $D_0 = 1.9 \times 10^{-3}$ m was generated
48
49 from hypodermic needles (BD Microlance, inner diameter $D_n = 1.5 \times 10^{-3}$ m) mounted on a 2D positioner
50
51 using a syringe pump (Cellix, World Precision Instruments, UK). The calculation of the droplet volume
52
53 was based on the numerical model proposed by Aminzadeh et al.⁵⁸. The droplets were released from
54
55 differently selected heights, H , with an initial velocity of zero to reach the desired velocities before their
56
57
58
59
60

1 impacts on the inclined solid surface. The inclination angle of the device surface was set to be 0°, 15°,
2
3 30°, 45°, and 60°. The impact and rebounding sequences were captured from a side view using a high-
4
5 speed camera (HotShot 1280CC) with a macro lens (120 mm BRAND) at 5000 frames per second (fps)
6
7 and a resolution of 432×244 pixels. MATLAB image processing tool was used to calculate the impact
8
9 velocity of the droplet from two consecutive images just before the its impact onto the device surface.
10
11 To fully understand how the SAW can modify the droplet impact on inclined surfaces, a set of systematic
12
13 experiments were performed to investigate the effects of inclination angle, impact velocity, and SAW
14
15 direction and power, at a lab temperature of 21 ± 0.5 °C and $50 \pm 5\%$ relative humidity. Under this
16
17 temperature, the density and surface tension of the DI water are $995 \text{ kg}\cdot\text{m}^{-3}$ and $0.072 \text{ N}\cdot\text{m}^{-1}$, respectively.
18
19 To confirm the repeatability of the experiments, each test was repeated four times.
20
21
22
23
24
25

26 **Uncertainty Analysis.** The diameter of the dispensing needle ($D_n=3\times 10^{-4}$ m) was captured and
27
28 measured, and the data were used to calibrate the images. A conversion factor of 40 $\mu\text{m}/\text{pixel}$ was
29
30 obtained. The resolution of the optical imaging system for observing droplets in our system was
31
32 determined to be 120 μm based on edge detection methods corresponding to three pixels. On the other
33
34 hand, the repeatability of the droplet diameter and impact velocity should be examined. Figure S3(a) in
35
36 the supplementary material shows that the uncertainty of the droplet diameter was $\pm 3.8\%$. In principle,
37
38 the impact velocity can be calculated by the equation, $U_0=\sqrt{2g(H - D_0)}$. The results of Figure S3(b) in
39
40 the supplementary material shows that the uncertainty of the impact velocity was $\pm 4.5\%$. The value of
41
42 the relative error of We number was calculated by the equation $\Delta We/We=\Delta D_0/D_0+2\Delta U_0/U_0$ to be 12.8%
43
44
45
46
47⁵⁹. The angle deviation of the SAW device holder was $\pm 0.3^\circ$.
48
49
50
51
52
53
54
55
56
57
58
59
60

RESULTS AND DISCUSSION

Impact Mechanism Based on Numerical Simulations. First of all, we simulate the impact and bouncing dynamics of a spherical droplet on a solid surface with an inclination angle of 30° at three cases for FI, USAW, and DSAW scenarios. For all the simulation cases, the droplet volume and impact velocity are kept constants at $3.5\mu\text{l}$ and 1.4 m/s , respectively. The details of the mathematical model (developed in OpenFOAM 4.x CFD toolbox), contact angle modeling, and numerical setup are presented in the Supplementary Material S4-S6. To validate the numerical results, a set of experiments with the same parameters was performed (the selected examples of the results for three cases are presented in Supplementary videos 1-3). A quantitative comparison between experimental and simulation results for the droplet contact width during the impact is shown in Figure 2(a). A good agreement between the experimental and numerical results can be found, proving that simulation results can be precisely used to analyze the effect of the SAW on droplet impact. Moreover, to qualitatively validate the numerical findings, comparisons between the droplet interfaces from both numerical and experimental results are presented in Supplementary Figure S4. Clearly, both the quantitative and qualitative comparisons show that the developed numerical method is capable of capturing the interaction between the acoustic waves and liquid medium, and also the TPCL movements.

As shown in Figure 2(a), the droplet continuously spread to its maximum diameter on the inclined surface for all three scenarios, and then the thickened rim starts to retract toward the center of the liquid. For the DSAW (USAW) scenario, the applied SAW energy restricts the tailing-edge (leading-edge) from spreading. For the FI scenario, the contact width reduces until the droplet is separated from the surface after 16.8 ms. By applying DSAW, the maximum spreading width and the time to reach this width are reduced (i.e., 2.4 ms compared to 3.6 ms for USAW and FI cases). After reaching the maximum spreading width, the contact width is gradually reduced until 8 ms after the onset of the impact. Then, it stays nearly a constant for ~ 2.6 ms since the droplet is moving on the inclined surface. Afterward, the

1
2 contact width is reduced sharply until the droplet is separated from the surface after 13.6 ms. For the
3
4 USAW case, during the whole retract phase, the contact width is lower (higher) than the FI (DSAW)
5
6 case. Moreover, the sharp reduction in spreading width is not observed at the end of the retracting phase
7
8 for the USAW scenario.
9

10
11 Figure 2(b) shows the average droplet velocity along the X-direction for the three cases. During the
12
13 spreading phase, the velocities do not show considerable differences. After ~ 2.8 ms from the onset of
14
15 impact, the droplet in the DSAW scenario starts to accelerate much faster than the other two scenarios.
16
17 In general, since the applied DSAW (USAW) energy promotes (restricts) the droplet motion in the X-
18
19 direction, the droplet has a higher (lower) average velocity compared to the FI scenario. The ratio of the
20
21 droplet tip height (highest point in Z-direction in liquid medium), Z , to its initial value, Z_0 (see Figure
22
23 2(c)) shows that the droplet tip heights have a rather similar behavior during the impact. However, since
24
25 the maximum spreading diameter of the droplet is larger for the FI scenario compared to those of USAW
26
27 and DSAW scenarios, the tip position of the liquid is lower for this case at its maximum spreading.
28
29
30
31
32
33
34
35
36
37
38
39
40
41
42
43
44
45
46
47
48
49
50
51
52
53
54
55
56
57
58
59
60

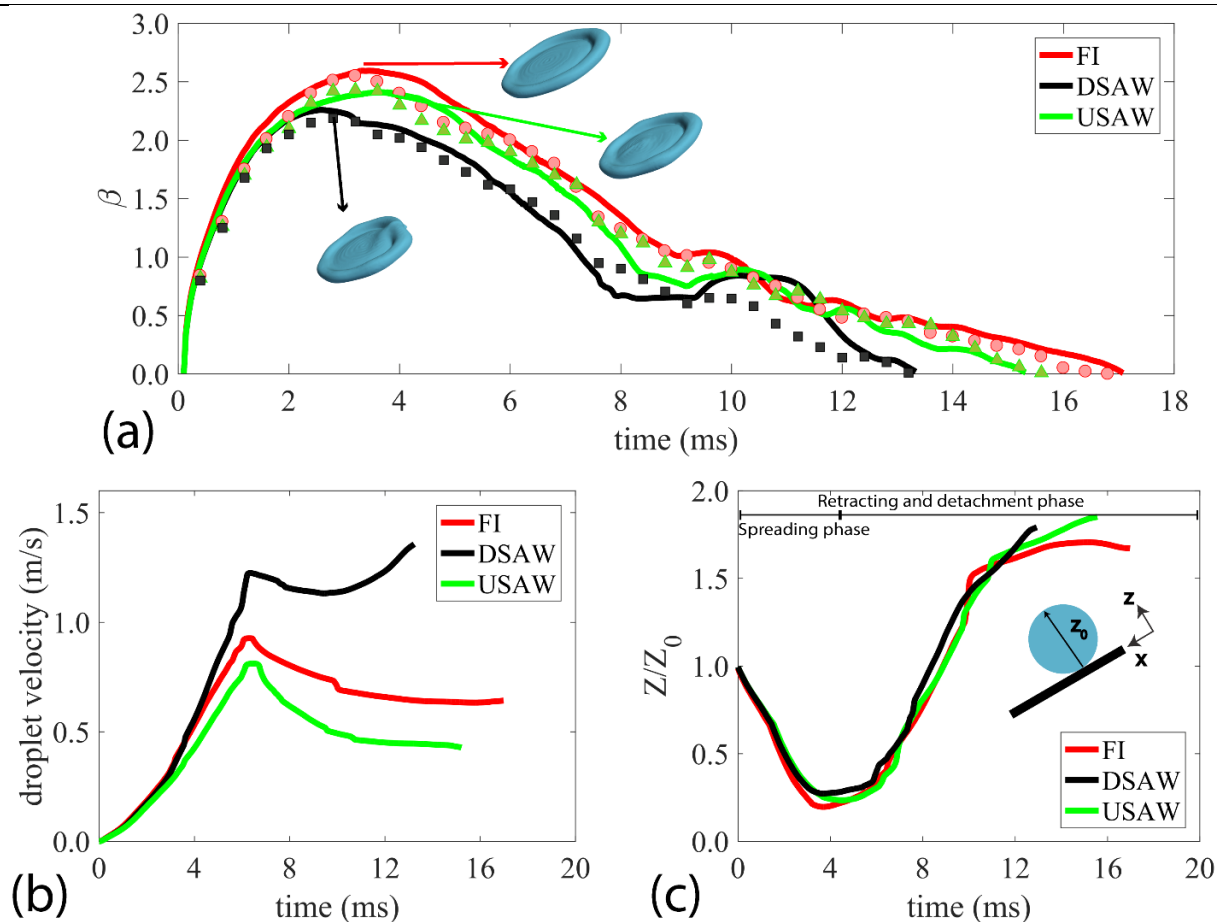


Figure 2. (a) A quantitative comparison between the simulation and experimental results for the droplet contact width evolution. (b) Temporal droplet velocity (i.e., an average of leading and tailing-edge velocities) in the X-direction. (c) Temporal evolution of normalized droplet tip height in Z-direction.

We then focus on the internal streaming patterns inside the liquid medium during the impingement for the designed three scenarios. Snapshots of internal streaming patterns in the middle plane of the droplet are illustrated in Figure 3. For the FI case, 2 ms after the onset of the impact, there is a strong velocity field in the region close to the leading-edge. However, due to viscous dissipation, this velocity field is not apparent in the tailing-edge, as shown in Figure 3(a). After 6 ms, while the leading-edge has moved ~ 1.4 mm on the inclined surface, the tailing-edge has moved as large as 3 mm, thus resulting in a

1
2 significant internal flow generation in the tailing-edge area (see Figure 3(a)). After 16 ms, near the last
3
4 moment of the impingement, the droplet contact width is minimized, and the internal streaming pattern
5
6 is faded compared to previous snapshots.
7

8
9 By applying USAW, after 2 ms from the onset of the impact, a hunch is noticeable in the center of the
10
11 spreading droplet on the inclined surface. Since the USAW is restricting the droplet to spread downward,
12
13 the velocity field in the leading-edge area is much weaker if compared to that of the FI case. After 6 ms,
14
15 the tailing-edge has moved ~ 2.6 mm. In the liquid medium close to the tailing-edge, a velocity field
16
17 along the X-direction is generated. Whereas near the center of the droplet, as a result of applied SAW
18
19 energy, a strong streaming pattern along Z-direction is observed, which can push the droplet upwards.
20
21 Finally, after 15 ms, the droplet is separated from the surface with a faded internal streaming pattern in
22
23 the area close to the droplet tip and a rather weak internal streaming field in the droplet root, mostly
24
25 along the Z-direction.
26
27

28
29 For the DSAW scenario (see Figure 3(c)), during the spreading phase, the SAW energy causes the
30
31 restriction of spreading from the tailing-edge, and a strong streaming pattern is created in the area close
32
33 to the tailing-edge. After 6 ms, the droplet tip height is 21% larger than that of the FI case (see
34
35 Figure 3(c)), and the internal streaming pattern in the droplet root is almost disappeared. However, a
36
37 strong velocity field is created in the droplet tip area. After 12.5 ms, the droplet is at its final moments
38
39 of impingement, and the liquid medium has a relatively strong velocity field inside.
40
41

42
43 The simulation results clearly show that the energy delivered by SAW has changed the internal
44
45 recirculation patterns upon the droplet impinging onto the inclined surfaces. By applying the USAW, in
46
47 all the stages of the impact, the velocity field (especially in the leading-edge area) is slightly rotated
48
49 toward Z-direction. However, the intensity of the internal streaming patterns looks similar to that of the
50
51 FI scenario. On the other hand, in the DSAW scenario, it is apparent that the liquid medium has a much
52
53 stronger internal recirculation pattern during the impact.
54
55
56
57
58
59
60

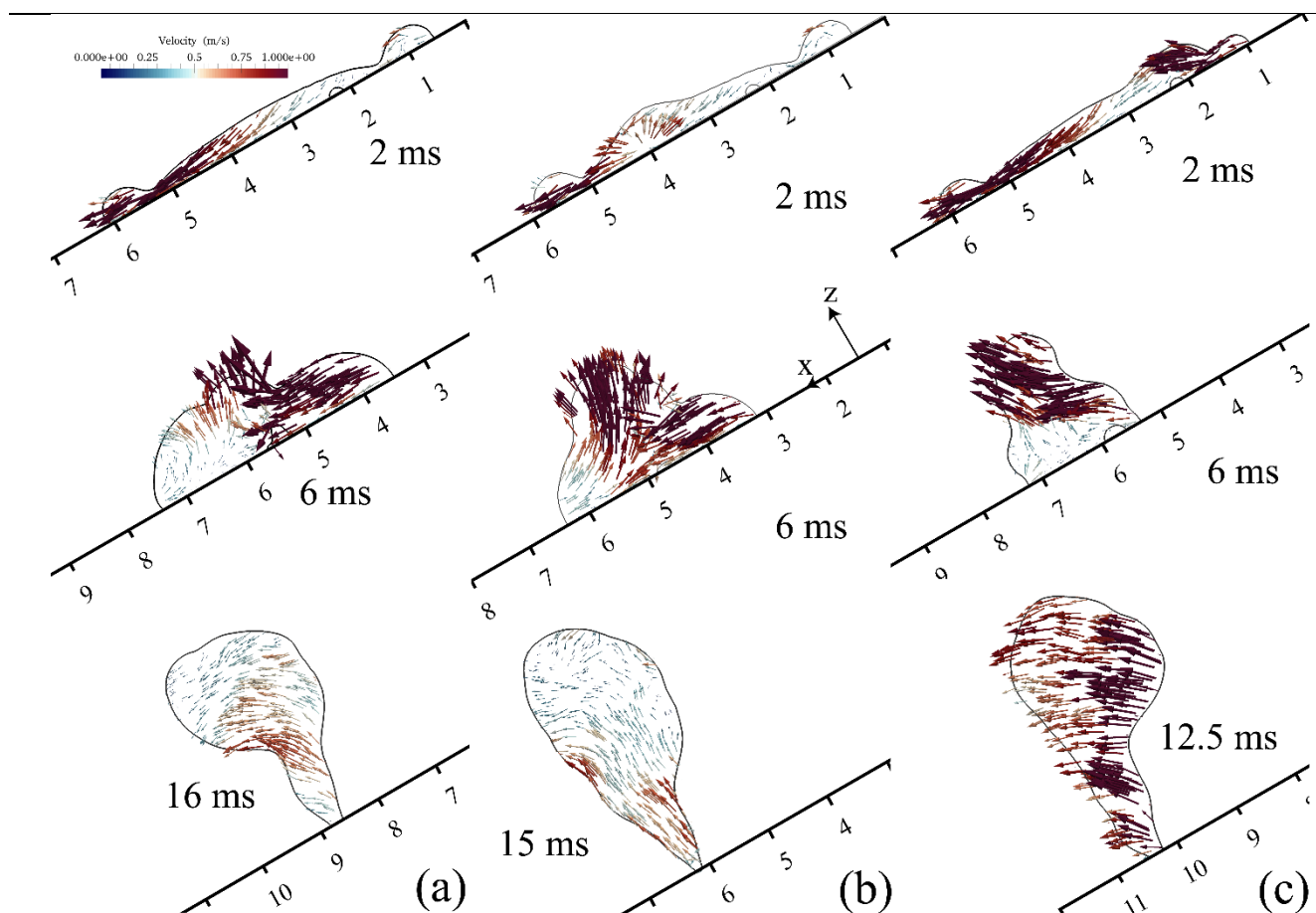


Figure 3. CFD snapshots of droplet interface overlaid by velocity vectors at spreading, retracting, and detachment stages for (a) FI scenario, (b) USAW scenario, and (c) DSAW scenario. For all the cases, a droplet with a volume of $3.5\mu\text{l}$ and We number of 50 is impacting on a surface with the inclination angle of 30° .

To quantitatively analyze the effect of the applied SAW energy, we further investigate the energy budget during the impact of the designed scenarios. During the droplet impact onto the inclined surfaces, gravitational, surface, and kinetic energies within the droplet are continuously converted among each other. Moreover, these energies are dissipated by liquid viscosity, wave generation at the gas-liquid interface, the interaction between solid and liquid phases, and sub-unit droplet separation^{28,60}. To reveal the physical differences among the above three scenarios, we analyze the kinetic energy, K , surface

energy, S , gravitational energy P , applied SAW energy, E_{SAW} , and energy dissipation by viscosity, E_{dis} obtained from the numerical simulations. The kinetic energy of the droplet can be defined as the volume integral of the kinetic energy of the infinitesimal volume element, V , within the liquid medium:

$$K = \int \frac{1}{2} \rho_l u^2 dV \quad (3)$$

where u is the magnitude of the liquid velocity. The surface energy S is given by:

$$S = \gamma_{LV} S_a + (\gamma_{SL} - \gamma_{SV}) S_s \quad (4)$$

where S_a and S_s are the areas of the droplet in contact with gas and solid medium, respectively. γ_{SV} and γ_{SL} are the surface tensions of the solid surface and solid-liquid interface. Gravitational energy, P , is defined based on the distance of each element in the Z -direction from the solid surface, z , and is calculated from

$$P = \int \rho_l g z dV \quad (5)$$

The total energy dissipation by liquid viscosity and applied SAW energy to the liquid medium can be defined as

$$E_{dis} = \int \int \frac{\mu}{2} (S_{ij} \cdot S_{ij}) dV dt \quad (6)$$

$$E_{SAW} = \int \int (\mathbf{f}_{SAW} \cdot \mathbf{U}) dV dt \quad (7)$$

where, $S_{ij} = \left(\frac{\partial u_j}{\partial x_i} + \frac{\partial u_i}{\partial x_j} \right)$ is the strain tensor⁶¹. Results of the evolution of energies for the simulated three scenarios are presented in Figure 4. All the energies in Figure 4 are normalized by the initial energy of the droplet at the onset of the impact (e.g., $E_0 = 1/2 \rho_l V_0 v_{impact}^2 + \gamma_{LV} A_0$, where V_0 , v_{impact} and A_0 are the volume, velocity and surface of the droplet at the impact moment). Results in Figure 4(b) show that the gravitational energy occupies less than $\sim 2\%$ of the total energy during the impingement for all the cases; therefore, it is not considered in the following analysis. Figure 4(c) illustrates the total energy dissipation from the impact moment.

1
2 For the FI scenario at the onset of the droplet impact, 79% of its total energy is in the form of kinetic
3 energy, and during the spreading phase (e.g., the blue area in Figures 4(a-c)), the kinetic energy is
4 converted to the surface energy or dissipated by viscous and capillary dissipation. During the droplet
5 spreading, surface energy is increased by 18%, and ~44% of the energy of the system is dissipated. At
6 the end of the spreading phase, there is a transient time when the surface energy stays almost a constant.
7 During the retraction phase, the surface energy is converted back to kinetic energy (e.g., the red area in
8 Figures 4(a-c)). At the end of the retraction phase, the surface energy is decreased by 23.3% from its
9 maximum, and the kinetic energy is increased by 7%. After ~7 ms, the kinetic energy of the droplet
10 starts to decrease due to the energy dissipation, and the droplet is separated from the surface after ~16.8
11 ms.

12
13 By applying the DSAW, the x-component of the SAW force along the inclined surface prevents the
14 tailing-edge from spreading, and thus, the maximum surface energy is ~4.2% lower than the FI case. On
15 the other hand, during the impingement, the total SAW energy, which is transferred to the liquid medium
16 (as shown in the small graph in Figure 4(a)), is as much as 66% of the initial energy of the droplet. The
17 kinetic energy of the droplet at the end of the spreading phase is decreased to ~20%, and the energy
18 dissipation is ~60%. However, as a result of applied SAW energy and conversion of the surface energy,
19 the kinetic energy of the droplet starts to increase sharply. Once all the energy stored as surface energy
20 is converted back to kinetic energy (i.e., after ~8 ms), the kinetic energy stays almost a constant, meaning
21 that the applied SAW energy is dissipated during this period. Due to the relatively higher kinetic energy
22 after the spreading stage, the droplet detaches from the surface after ~13.6 ms, which is 20% shorter in
23 contact time than the FI case.

24
25 For the USAW case, during the 6 ms after the onset of the impact, the kinetic energy has a rather
26 similar trend to the FI scenario. Nevertheless, between 6-10 ms after the impact, the kinetic energy of
27 the droplet is ~5% higher on average than that of the FI case. The results indicate that despite the applied
28 SAW energy to the droplet for both USAW and DSAW scenarios are equal (see the embedded graph in

1
2 Figure 4(a)), the droplet gains less kinetic energy in the USAW cases due to significant energy
3
4 dissipation. This can be explained by the fact that the x-component of the SAW force is in the reverse
5
6 direction of the component of gravitational force and thus (as a result of interaction between these forces
7
8 in a 3D pattern) a rather strong internal recirculation field with vortices is generated within the liquid
9
10 medium, thus dissipating more energy. Interestingly, for the USAW case, the amount of dissipated
11
12 energy by viscosity is higher than the initial droplet energy. The ratio of the total dissipated energy for
13
14 USAW and DSAW cases, $\frac{E_{disUSAW}}{E_{disDSAW}}$ is ~ 1.35 . This result is significant since it shows that by changing
15
16 the direction of the SAW propagation, energy dissipation within the liquid and kinetic energy of the
17
18 droplet can be modified.
19
20
21
22

23 By comparing the simulation results from the above three scenarios on the inclined angled plate, we
24
25 can conclude that by changing the direction of the applied SAW, the amount of kinetic energy and energy
26
27 dissipation during the impingement can be altered to control impact parameters such as contact time,
28
29 and droplet movement on the surface during the impact. After understanding the physics behind the
30
31 effect of SAW on the droplet impact on the inclined surface, we then experimentally investigated the
32
33 effects of surface acoustic waves on the impact dynamics.
34
35
36
37
38
39
40
41
42
43
44
45
46
47
48
49
50
51
52
53
54
55
56
57
58
59
60

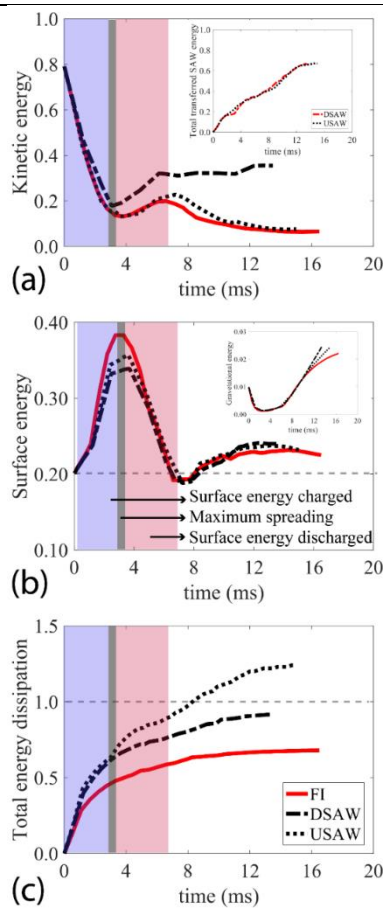


Figure 4. Simulation results of the effect of SAW on the temporal evolution of energy. (a) The normalized kinetic energy of the liquid medium. The embedded graph represents the total energy of the droplet. (b) The normalized surface energy of the liquid. Normalized gravitational energy is presented in the embedded graph. (c) Energy dissipation during the impingement. Blue and red areas represent the droplet spreading and retracting, respectively. All the energies are normalized with the total droplet energy at the inset of the impact.

Droplet Impact Phenomena from Experimental Results. Figure 5 shows snapshot examples of the impact of a droplet with a volume of $3.5 \mu\text{l}$ and a Weber number of ~ 30.3 on a surface with an inclination angle of 15° , for the designed three scenarios. For the FI case (see Figure 5(a)), the droplet first spreads to its maximum diameter forming a crater shape, and then the rim starts to retract toward the center. In this case, the kinetic energy of the droplet at the end of the retraction phase is not large enough to detach

the whole droplet from the surface, thus leading to deposition of the droplet after a series of vibration on the surface.

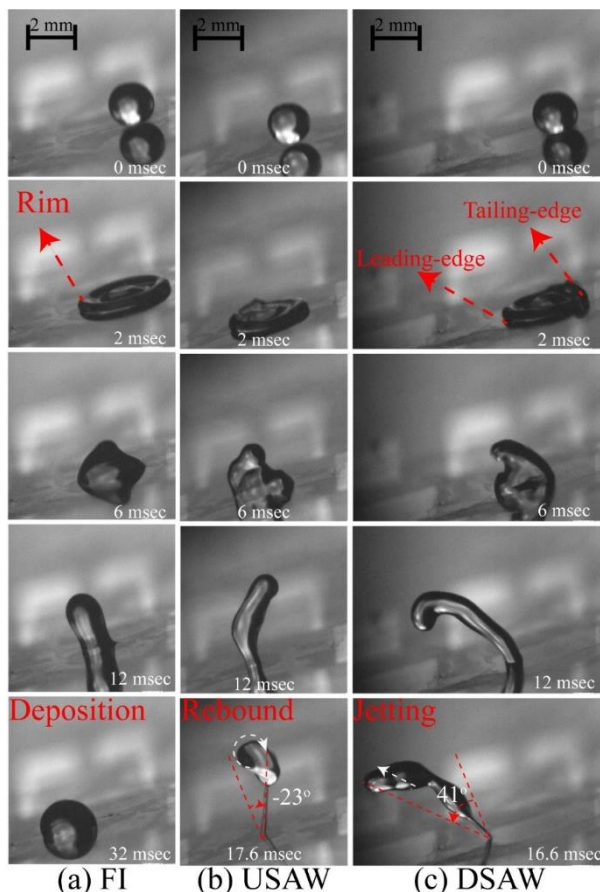


Figure 5. Sequential snapshots of a water droplet impacting on the solid surface with an inclination angle of 15° and a Weber number of 30.3 for (a) FI scenario, (b) USAW scenario with the power of 15 W applied to the IDTs, (c) DSAW with the power of 15 W applied to the IDTs. In all the scenarios, DI water droplet with a volume of $3.5 \mu\text{l}$ is impacting on the hydrophobic surface of the SAW device. See the supplementary videos V4-V6 for the experimental movies.

On the other hand, from our numerical results, we know that by applying the USAWs or DSAW onto the inclined devices, the energy budget of the droplet is changed (depending on the SAW power), and

1
2 correspondingly the droplet dynamics and impact regime are changed. As shown in Figure 5(b), the
3
4 applied USAW deforms the leading-edge of the droplet during the spreading phase, and after ~6 ms, a
5
6 liquid beam starts to form at the end of retracting phase. As discussed in the numerical results, the
7
8 USAW can slightly increase the kinetic energy of the droplet during the impingement process. As a
9
10 result, the droplet is detached from the surface after ~18 ms in a rotating sphere shape (see Figure 5(b)).
11
12 More interestingly, by applying DSAW, the tailing-edge is deformed during the spreading phase, and
13
14 the kinetic energy of the liquid is intensively increased, leading to a liquid beam formation after ~10 ms.
15
16 The enhanced jet is separated from the surface along a rebounding angle of 41° after ~17 ms. The time
17
18 evolution plot of the droplet contact line width is illustrated in Supplementary Figure S6(a). The
19
20 comparisons between these three cases show that by applying the SAWs, critical parameters of droplet
21
22 impact such as contact time, impact regime, and rebounding angle can practically be modified.
23
24
25

26
27 **Effects of Inclination Angle on Impact Dynamics.** To understand the effects of inclination angle on
28
29 the impact dynamics in the presence of SAW, a set of experiments were conducted using the DI water
30
31 droplets with a volume of $3.5 \mu\text{l}$ and an impact velocity of 1.4 m/s. The obtained distribution maps of
32
33 droplet impact regimes for the cases of USAW and DSAW are shown in Figures 6(a-b), respectively.
34
35 The impact regimes are categorized into droplet deposition, partial and complete rebound, jetting
36
37 rebound, and break up (see supplementary Figure S7).
38
39
40

41 In the absence of SAW and at a low inclination angle (e.g., 15° and less in this study), the droplet
42
43 cannot be detached from the surface after the impact. However, by increasing the inclination angle above
44
45 15° , the droplet can be fully detached from the surface in the FI scenarios. As the inclination angle
46
47 increases, the tangential component of the gravitational force is increased (as illustrated in Figure 1(d)).
48
49 Accordingly, the droplet has more kinetic energy during the retracting phase, which results in full
50
51 detachment of the droplet from the surface.
52
53

54
55 By applying SAWs during the droplet impacting inclined surfaces, the impact regime can be changed
56
57 among rebound, jetting, or droplet break-up with the gradual increase of applied powers. For the DSAW
58
59

1 cases, by applying SAWs with high powers (i.e., with powers higher than 25 W applied to the IDTs), the
2 liquid droplet is bounced off the solid surface as a thin beam. However, droplet break-up into several
3
4 liquid droplet is bounced off the solid surface as a thin beam. However, droplet break-up into several
5
6 sub-units is sometimes observed in the USAW cases at very high applied powers. In these cases, the
7
8 droplet starts to break-up after reaching the maximum diameter since the surface tension force cannot
9
10 overcome the applied SAW momentum, which has been transferred into the liquid medium.
11
12

13 The corresponding contact times for the designed experiments are presented in Figure 6(c-d). As
14 discussed, for inclination angles of 0° and 15° , the droplet stays stationary on the inclined surface at the
15
16 end of the retract phase, and thus the contact time is defined as indefinite for these cases. Nevertheless,
17
18 SAWs can change the droplet impact regime from deposition to complete rebound or jetting from the
19
20 surface. Moreover, by increasing the applied SAW power at each fixed inclination angle, the droplet
21
22 contact time is reduced. The detailed analysis shows that the contact time can be effectively reduced by
23
24 applying SAW. For instance, as shown in Figure 6(d), for the surface inclination angle of 45° by applying
25
26 DSAW with the power of 35 W , the contact time can be reduced as much as 30% compared to the FI
27
28 scenario. From the simulation results, we know that by applying SAWs (both the USAW and DSAW),
29
30 the energy budget of the droplet is changed, and the droplet gains more kinetic energy during the retract
31
32 phase to bounce off the inclined surface.
33
34
35
36
37
38
39
40
41
42
43
44
45
46
47
48
49
50
51
52
53
54
55
56
57
58
59
60

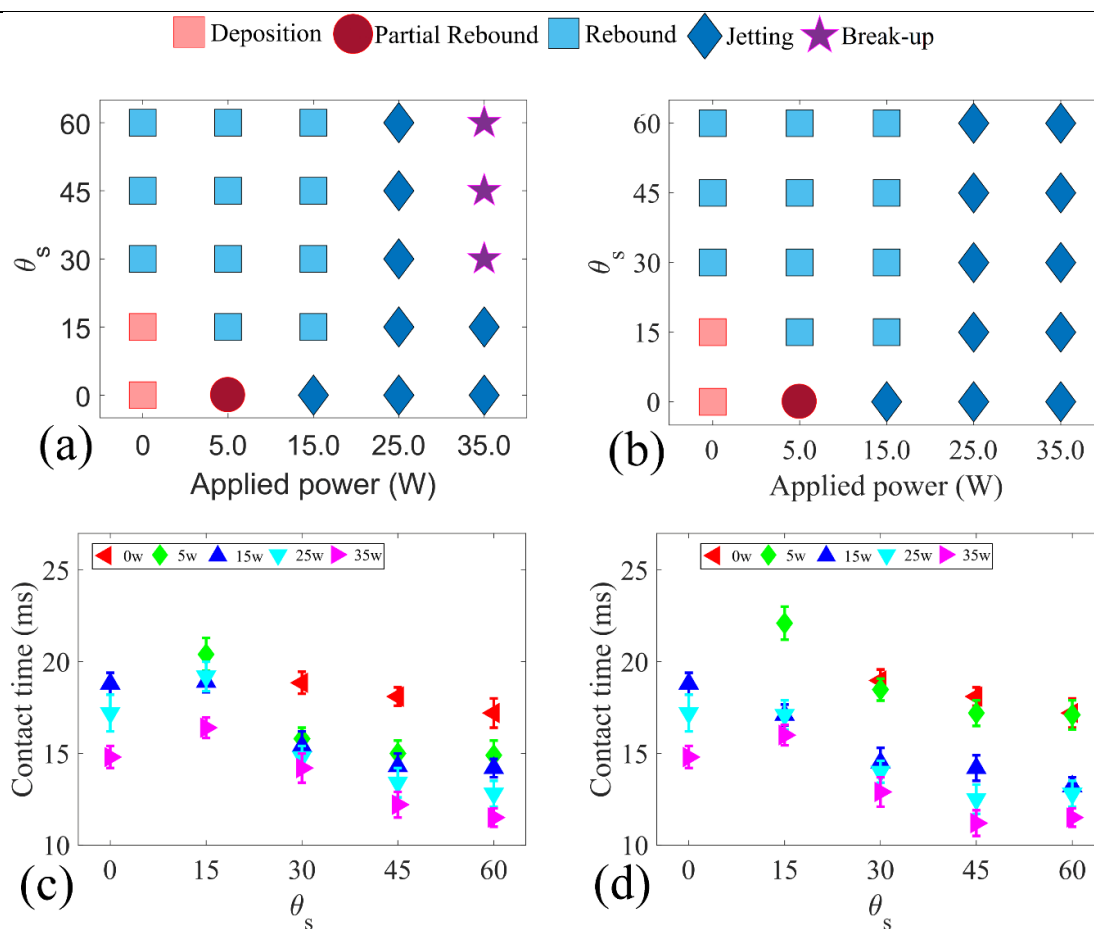


Figure 6. (a) Droplet impact regime map as a factor of applied SAW power and surface inclination angle for (a) USAW, and (b) DSAW scenarios. Contact time versus inclination angle for different applied SAW powers for (c) USAW, and (d) DSAW scenarios. Note that the contact time is not shown for the deposition and partial rebound cases. In all the cases, the droplet with a volume of $3.5\mu\text{l}$ and Weber number of 50 impacts on the ZnO/Si SAW device.

Figure 7 presents the effect of inclination angle on maximum spreading diameter β_{max} , rebounding angle, and movement along the surface. As shown in Figures 7(a) and (d), by increasing the inclination angle for the FI scenarios, the value of β_{max} increases. For all the scenarios, by increasing the inclination angle, the tangential component of the gravitational force, $mg\sin\theta_s$, enhances the spreading of the droplet front but suppresses the spreading of the back of the droplet. However, when the SAWs are

1 applied, the tangential component of the SAW force, $f_{SAW} \sin \theta_R$, limits the spreading of the droplet (e.g.,
2 the leading edge for USAW and the tailing edge for DSAW). At a lower inclination angle, the SAW
3 force is dominated in limiting the spreading of the droplet. However, by increasing the inclination angle,
4 the leading edge for USAW and the tailing edge for DSAW). At a lower inclination angle, the SAW
5 force is dominated in limiting the spreading of the droplet. However, by increasing the inclination angle,
6 the gravitational force becomes dominant, which leads to larger values of the maximum spreading
7 diameters (see Figure S1 in supplementary material). The maximum spreading is reduced more by
8 applying USAW compared to DSAW for all the angles.

15 Results of the droplet rebounding angles (see Figure 1 for definition) are illustrated in Figures 7(b)
16 and 7(e). In general, the interaction between the applied SAW force and the gravitational force
17 determines the rebounding angle of the droplet. For the FI scenarios, since the only force redirecting the
18 droplet during the rebounding is gravity, the rebounding angle of the droplet has a nearly linear trend as
19 a function of inclined angle (see the dashed red line in Figure 7(b) and 7(e)). However, by applying
20 lower SAW powers to the IDTs (i.e., 5-15 W), the interactions among these forces and the corresponding
21 rebounding angles are modified compared those of FI cases. At higher powers, the droplet is fully
22 detached from the surface along the Rayleigh angle. The results show that at higher powers, the SAW
23 force is large enough compared to the gravitational force, and will drive the droplet as a jet along the
24 Rayleigh angle of the SAW device along the inclined solid surface regardless of the inclination angle.
25 These results show that, by changing the SAW power and direction on any inclination angle, the droplet
26 rebounding angle can be changed. To examine the repeatability of the jet redirecting by SAW, droplet
27 impact with We number of 50 on a surface with an inclination angle of 15° was repeated 16 times, while
28 a power of 25 W was applied to the IDTs. The histogram results of the tests are presented in Figure S8
29 of the supplementary materials, which showed good repeatability.

30 Figures 7(c) and 7(f) show the results of distances for droplet movements along the X-direction, δ ,
31 between the impact and detachment. As explain by the simulation results, for the DSAW cases, the
32 tangential components of SAW and gravitational force tend to move forward the droplet in the X-
33 direction, therefore, by increasing the SAW power or inclination angle, the value of δ increases.

1
2 However, in the USAW cases, the tangential components of gravitational and SAW forces work against
3
4 each other, and the value of δ is decreased by increasing the SAW power.
5

6 **Effect of Droplet Impact Velocity.** Figure 8(a-b) present the results of the impact regime map as a
7
8 function of We number and SAW applied power, with the droplet volume and inclination angle of the
9
10 surface fixed at 3.5 μL and 15° . For the DI cases and at lower We numbers (i.e., 10 and 30), the droplet
11
12 stays stationary on the surface after the impact, and the contact time is indefinite. By increasing the We
13
14 number to 50, since the initial kinetic energy of the droplet is increased, part of the droplet gains enough
15
16 energy at the end of the retract phase to be detached from the surface. However, the droplet root still
17
18 stays in contact with the surface. At higher We numbers, the liquid kinetic energy at the end of the retract
19
20 phase is high enough to detach the whole droplet from the solid surface, so a complete rebound is
21
22 observed.
23
24
25
26

27 For both the USAW and DSAW scenarios, jetting rebound is observed when the applied SAW power
28
29 is larger than 20 W . At these larger SAW powers, the kinetic energy induced by the SAWs is much
30
31 higher than the dissipation energy due to the liquid viscosity. Correspondingly, the droplet has enough
32
33 energy to be separated from the solid surface at the end of the retract phase. Conversely, for the USAW
34
35 scenario and the applied SAW power of 15 W , a complete rebound of the droplet from the surface is
36
37 observed for all the We numbers except the We number of 70. This inconsistency is due to the relatively
38
39 more viscous dissipation in this case, where the opposite directions of the momentums generated by
40
41 gravitational and SAW forces during the spreading phase cause significant vortices within the droplet.
42
43 These vortices, in turn, dissipated the kinetic energy of the droplet. Therefore, the kinetic energy of the
44
45 droplet might not be high enough at the retract phase to detach the liquid phase from the solid surface.
46
47
48
49
50
51
52
53
54
55
56
57
58
59
60

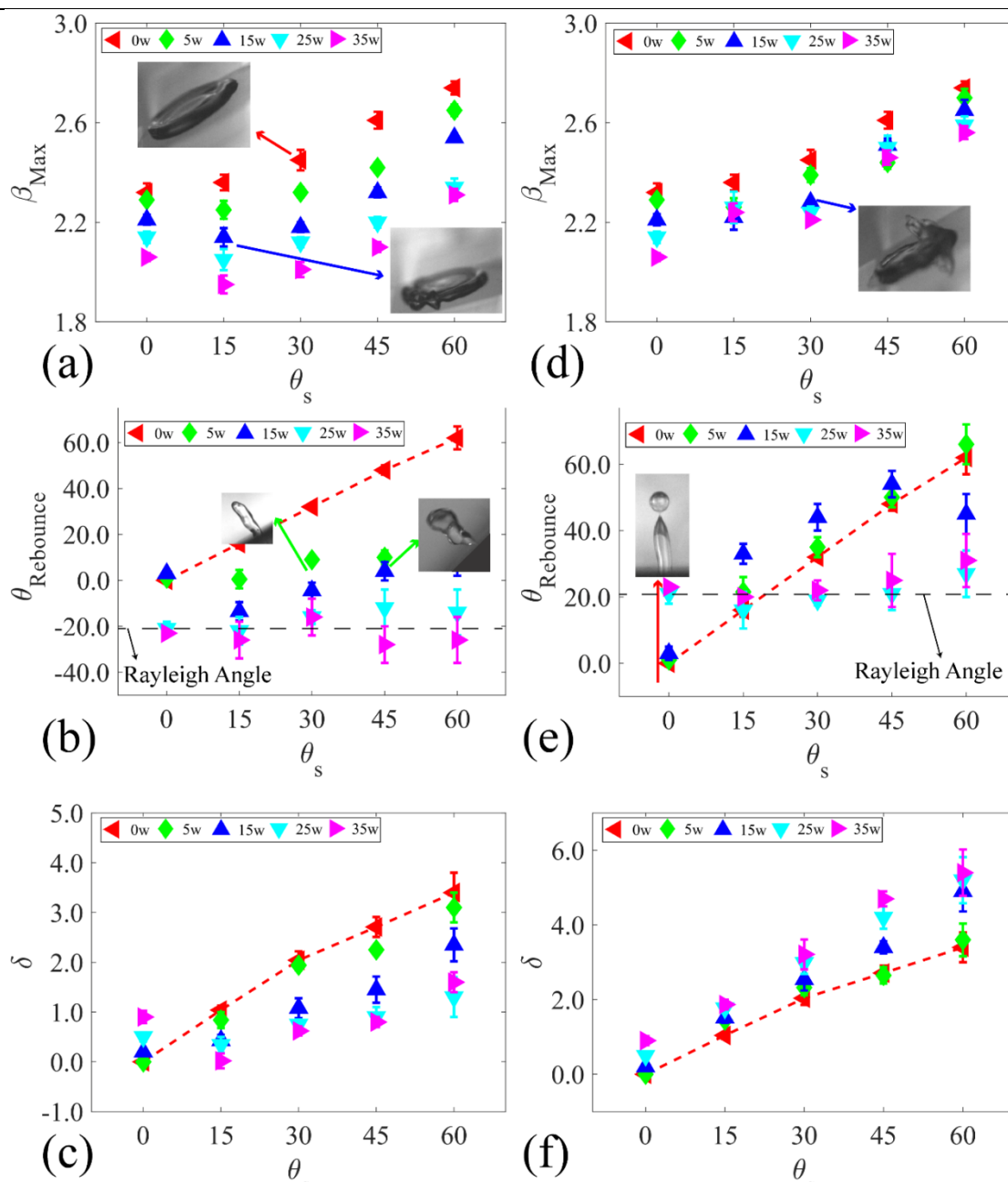


Figure 7. Effect of surface inclination angle on (a) maximum spreading, (b) Rebounding angle, and (c) Droplet movement along X direction for USAW scenario. Effect of surface inclination angle on (d) maximum spreading, (e) Rebounding angle, and (f) Droplet movement along X direction for DSAW scenario. In all the cases, the droplet with a volume of $3.5\mu\text{l}$ and a Weber number of 50 is impacted on a ZnO/Si SAW device.

In order to investigate the effect of SAWs on droplet dynamics, the contact times of the droplet as a function of We numbers were obtained, and the results are presented in Figure 8 (c-d). Comparisons of these two graphs with Figure 8 (a-b) reveal that for the impacts with We number lower than 70 and FI scenarios, the droplet is deposited on the surface. However, by applying SAWs with powers higher than 25 W , regardless of the SAW direction, a complete detachment of the droplet from the surface is observed. Interestingly, results show that the contact time of the droplet can be reduced by the factor of a maximum of 48.5% by increasing the SAW power to 35 W .

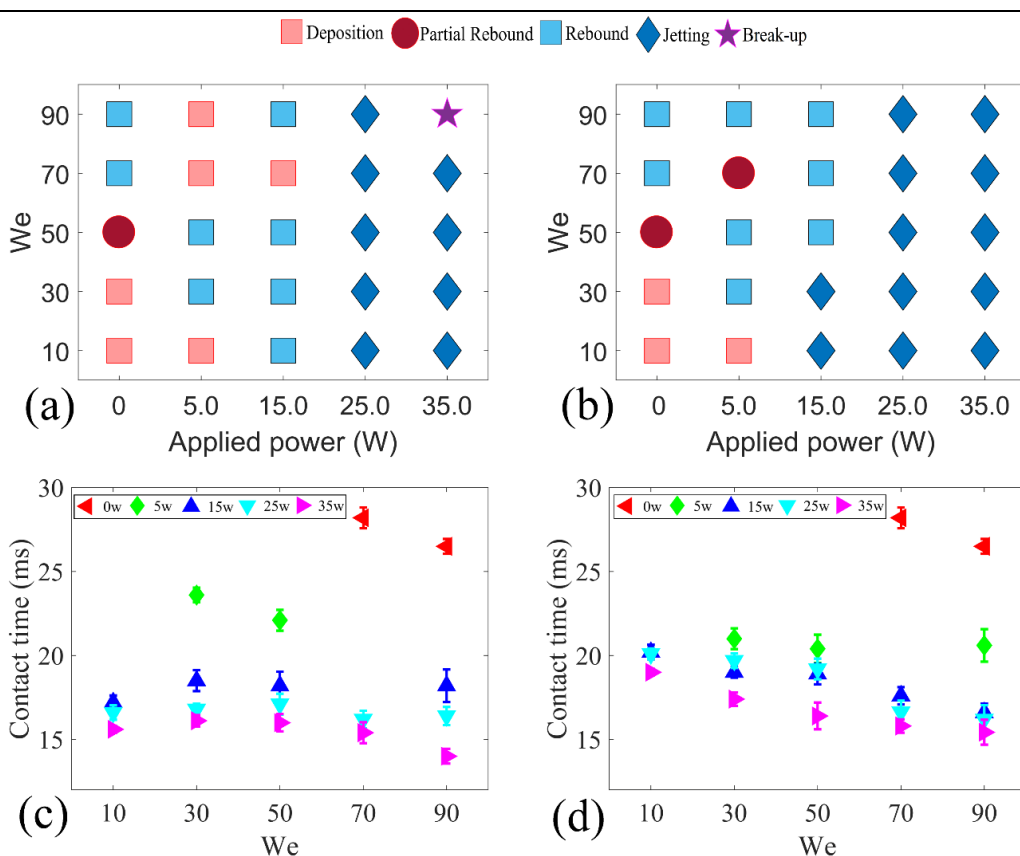


Figure 8. Droplet impact regime map as functions of applied SAW power and We number for (a) USAW, and (b) DSAW cases. Contact time versus We number for different applied SAW powers for (c) USAW, and (d) DSAW scenarios. In all the experiments, a droplet with a volume of $3.5\mu\text{l}$ is impacting on a ZnO/Si SAW device with an inclination angle of 15° .

1
2 Figure 9(a) and 9(d) show the effects of We number on maximum spreading widths of the droplet
3 during the impact for the scenarios. Due to increased initial kinetic energy, the value of β_{Max} for FI
4 scenarios is increased as We number is increased. However, by applying the SAWs, the droplet spreading
5 width is limited, and thus the value of β_{Max} is decreased. For both USAW and DSAW scenarios and
6 regardless of the We number, the maximum spreading distance is decreased by increasing the applied
7 SAW power. This is due to the restriction of the contact line motion during the spreading phase in the
8 area due to the applied SAWs.
9

10
11 The effect of We number on rebounding angle is illustrated in Figure 9(b) and 9(e). It is apparent from
12 these figures that by changing the SAW direction, the direction of the detached droplet is changed. For
13 the DSAW case, as expected, by increasing the applied SAW power, the rebounding angle is increased.
14 On the contrary, for the USAW cases, the rebounding angle is decreased significantly by changing the
15 applied power. It is interesting to observe that a wide-range of the rebounding angle up to 110° (e.g.,
16 from -60° to 50°) can be achieved by changing the applied SAW power and direction.
17

18
19 Figure 9(c) and 9(f) show the effect of We number on the values of displacement δ . For the FI scenario,
20 with the successive increases in the We number, as a result of the increase in the tangential component
21 of the gravitational force, the value of δ increases linearly. After applying the DSAW, the tangential
22 component of the SAW force enhances the movement of the droplet in the X-direction, and the value of
23 distance δ increases significantly. For the USAW scenarios, the tangential components of the
24 gravitational and SAW forces are in opposite directions, and the interaction between these forces
25 determines the displacement of δ values. Here, using a standard equation of $\delta = AWe^B$ we obtained the
26 regression fitting for the movement of the droplet on the surface in FI scenarios with $A = 0.1$ and $B =$
27 0.61 , as shown with the dashed lines in Figure 9(c) and 9(f).
28
29
30
31
32
33
34
35
36
37
38
39
40
41
42
43
44
45
46
47
48
49
50
51
52
53
54
55
56
57
58
59
60

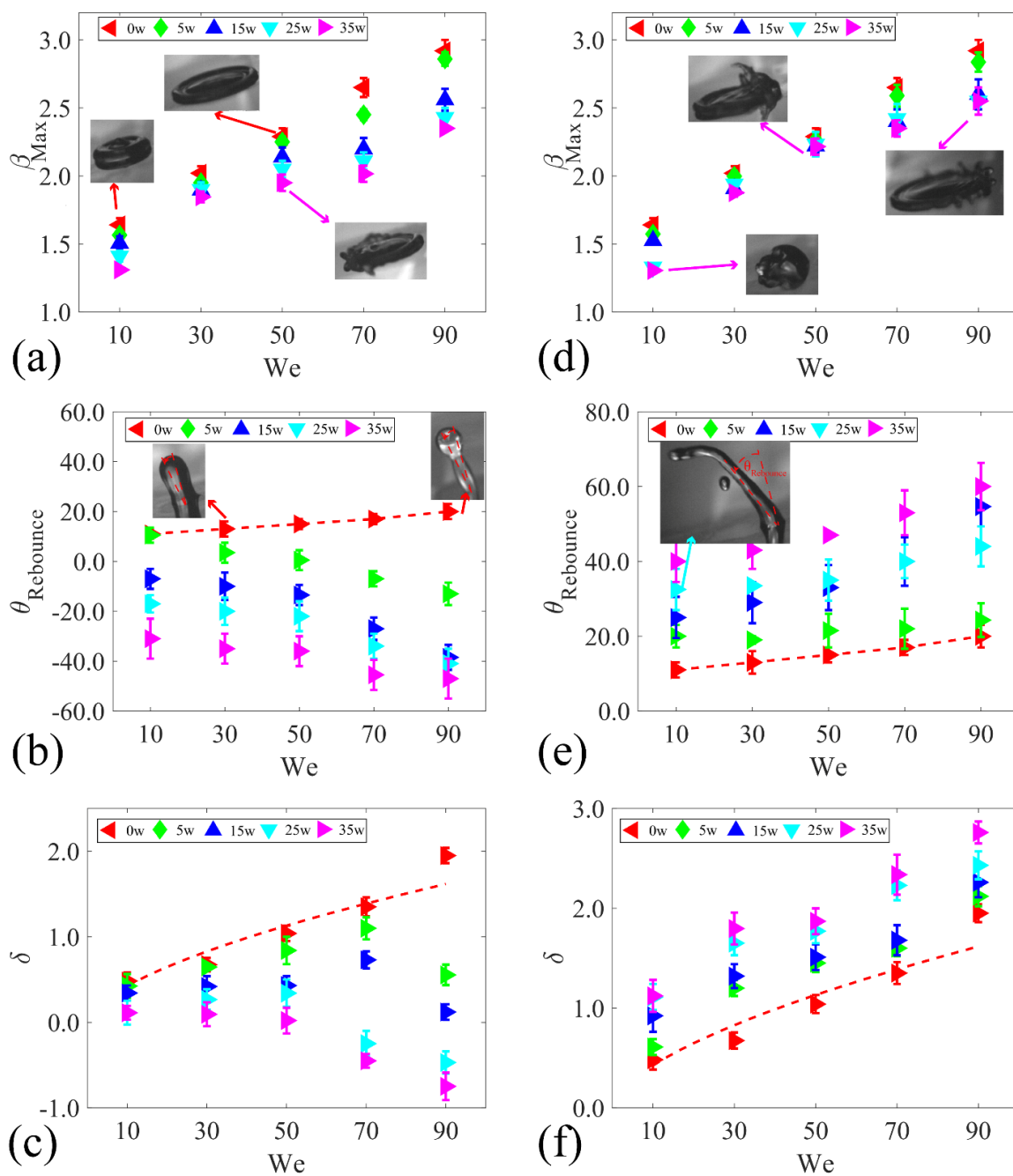


Figure 9. Effect of impact velocity on (a) maximum spreading, (b) Rebounding angle, and (c) Droplet movement along X direction for USAW scenario. Effect of impact velocity on (d) maximum spreading, (e) Rebounding angle, and (f) Droplet movement along X direction for DSAW scenario.

1
2 In all the cases, the droplet with a volume of 3.5 μ l impacts a ZnO/Si SAW device with a surface
3
4 inclination angle of 15 $^{\circ}$.
5
6
7

8 9 10 CONCLUSION

11
12
13
14 In summary, the potential of applying SAWs to modify the droplet impact dynamics on inclined
15 surfaces is investigated in this paper. We have experimentally and numerically studied the effects of
16 impact velocity, SAW direction and power, and surface inclination angle on the droplets impact behavior
17
18 on a hydrophobic surface. Numerical results verified that SAWs could alter the energy budget of the
19
20 impacting droplet, and modify the impact dynamics. Applying the DSAW to the surface during the
21
22 impingement process increases the kinetic energy of the droplet, leading to a faster detachment from the
23
24 surface. On the other hand, by applying the USAW, the energy dissipation within the liquid medium is
25
26 increased compared to those for the DSAW and FI scenarios. The slightly increased kinetic energy
27
28 causes a faster detachment from the surface. Effects of SAW directions, substrate inclination angle, and
29
30 impact velocity on the hydrodynamics of the droplet were examined and discussed in terms of droplet
31
32 impact regime, contact time, maximum spreading, rebounding angle and droplet movement on the
33
34 surface during the impact. Applying the SAWs, regardless of its direction, can avoid the droplet to
35
36 deposit on the inclined surface after the impact. This result shows the great potential of the SAW for
37
38 applications in smart water-repellent surfaces.
39
40
41
42
43
44
45

46 Moreover, droplet contact time can be modified and controlled in a certain range by changing the
47
48 power and direction of the propagating SAWs on the solid surface. Contact time control (not only
49
50 reduction) is important for applications, such as spray cooling of reactors and electronic components.
51
52 The presented simulation and experimental results show that using the SAWs, the contact time of the
53
54 droplet on the inclined surfaces can be actively modified in a wide range. Additionally, droplet
55
56
57
58
59
60

1
2 rebounding angles are varied by changing the SAW power and direction. Directing the droplet toward a
3
4 certain target after impact onto an inclined surface could be useful in microfluidic applications such as
5
6 3D bio-printing. Our experimental results show that the rebounding angle of the droplet can be modified
7
8 effectively for different impact situations. Thus, the results illustrate the significant effect of acoustic
9
10 waves on droplet impact on inclined surfaces. Therefore, we expect that SAW technology can be used
11
12 in many applications such as smart self-cleaning, anti-icing, and anti-infection surfaces.
13
14
15
16
17

18 ASSOCIATED CONTENT

19 20 **Supporting Information.**

21
22
23 S1. Showing the effect of inclination angle and SAW direction on the interaction between gravitational
24
25 and SAW forces.
26
27

28 Figure S10. Schematic views of the effects of SAW direction and inclination angle on the interaction
29
30 of SAW and gravitational forces.
31
32

33 S2. Illustration of the experimental setup

34
35
36 Figure S2. (a) Schematic view of the SAW device, (b) Schematic illustration of the experimental
37
38 setup
39
40

41
42 Figure S3. Scanning electron microscopy (SEM) image of the ZnO/Si SAW device surface.
43
44

45 S3. Uncertainty analysis

46
47
48 Figure S4. Uncertainty analysis for (a) Droplet initial diameter D_0 ; and (b) droplet impact velocity U_0
49
50 for different experimental cases as a function of droplet release height, H .
51
52

53 S4. Explaining the mathematical modeling.

54
55
56 S5. Explaining the developed contact angle modeling.
57
58

1
2 S6. Explaining the numerical setup.
3

4
5 Table SI. Input parameters and modeling setup for numerical simulation
6

7
8 S7. Explaining the model validation.
9

10
11 Figure S5. Comparisons between experimental and simulation results of the droplet interface during
12 the impact on a surface with an inclination angle of 30° for (a) FI scenario, (b) USAW scenario, and (c)
13 DSAW scenario. In both simulation and experiments, a droplet with a volume of $3.5 \mu\text{l}$ and We number
14 of 50 is impacting on the surface.
15
16
17
18
19

20
21 S8. Analysis of dynamic contact angle
22

23
24 Figure S6. (a) Droplet normalized contact width versus time. Lines are provided as a guide for the
25 eyes. Temporal evolution of apparent dynamic contact angle of leading and trailing edges for (b) FI
26 scenario, (c) USAW scenario, (d) DSAW scenario.
27
28
29

30
31 Figure S7. Showing the different impact regimes.
32

33
34 Figure S8. Showing the repeatability of the droplet rebounding angle from the surface.
35

36
37 Video S1 showing the droplet free impact on a smooth hydrophobic surface with an inclination angle
38 of 30° with $We = 50$ (MP4).
39
40

41
42 Video S2 showing the droplet impact in the presence of USAW with the power of 15 W (applied to
43 the IDTs) on a smooth hydrophobic surface with an inclination angle of 30° with $We = 50$ (MP4).
44
45

46
47 Video S3 showing the droplet impact in the presence of DSAW with the power of 15 W (applied to
48 the IDTs) on a smooth hydrophobic surface with an inclination angle of 30° with $We = 50$ (MP4).
49
50

51
52 Video S4 showing the droplet free impact on a smooth hydrophobic surface with an inclination angle
53 of 15° with $We = 30$ (MP4).
54
55
56

1
2 Video S5 showing the droplet impact in the presence of USAW with the power of 15 W (applied to
3 the IDTs) on a smooth hydrophobic surface with an inclination angle of 15° with $We = 30$ (MP4).
4
5

6
7 Video S6 showing the droplet impact in the presence of DSAW with the power of 15 W (applied to
8 the IDTs) on a smooth hydrophobic surface with an inclination angle of 15° with $We = 30$ (MP4).
9
10

11 12 13 AUTHOR INFORMATION

14 15 **Corresponding Author**

16
17
18 *Email: richard.fu@northumbria.ac.uk;
19
20

21 22 **ORCID**

23
24 Mehdi H. Biroun: 0000-0003-3269-7749

25
26 Mohammad Rahmati: 0000-0003-4903-5370

27
28 Ran Tao: 0000-0001-5461-5930

29
30 Hamdi Torun: 0000-0002-7882-286X

31
32 Mehdi Jangi: 0000-0001-7318-8698

33
34 Y.Q. Fu: 0000-0001-9797-4036
35
36
37

38 39 **Notes**

40
41 The authors declare no conflict of interest.
42

43 44 **ACKNOWLEDGMENTS**

45
46 The UK Engineering and Physical Sciences Research Council (EPSRC) grants EP/P018998/1, Special
47 Interest Group of Acoustofluidics from UK Fluids Network (EP/N032934/1), Newton Mobility Grant
48 (IE161019) through Royal Society and the National Natural Science Foundation of China.
49
50

51 52 53 **ABBREVIATIONS**

54
55
56
57
58
59
60

1
2 SAW, surface acoustic wave; DSAW, downward surface acoustic wave; USAW, upward surface
3
4 acoustic wave; FI, free impact; TPCL, three-phase contact line; CLSVOF, couples level set volume of
5
6 fluid; IDT, interdigital transducer; CFD, computational fluid dynamics,
7

8
9 REFERENCES

- 10
11
12 (1) Lai, Y.; Tang, Y.; Gong, J.; Gong, D.; Chi, L.; Lin, C.; Chen, Z. Transparent
13
14 Superhydrophobic/Superhydrophilic TiO₂-Based Coatings for Self-Cleaning and Anti-Fogging. *J.*
15
16 *Mater. Chem.* **2012**, *22* (15), 7420–7426. <https://doi.org/10.1039/c2jm16298a>.
17
18
19
20 (2) Mishchenko, L.; Hatton, B.; Bahadur, V.; Taylor, J. A.; Krupenkin, T.; Aizenberg, J. Design of Ice-
21
22 Free Nanostructured Surfaces Based on Repulsion of Impacting Water Droplets. *ACS Nano* **2010**,
23
24 *4* (12), 7699–7707. <https://doi.org/10.1021/nn102557p>.
25
26
27
28 (3) Kreder, M. J.; Alvarenga, J.; Kim, P.; Aizenberg, J. Design of Anti-Icing Surfaces: Smooth, Textured
29
30 or Slippery? *Nature Reviews Materials*. Nature Publishing Group January 11, 2016.
31
32 <https://doi.org/10.1038/natrevmats.2015.3>.
33
34
35
36 (4) Cao, L.; Jones, A. K.; Sikka, V. K.; Wu, J.; Gao, D. Anti-Icing Superhydrophobic Coatings. *Langmuir*
37
38 **2009**, *25* (21), 12444–12448. <https://doi.org/10.1021/la902882b>.
39
40
41
42 (5) Zhang, L.; Wu, J.; Hedhili, M. N.; Yang, X.; Wang, P. Inkjet Printing for Direct Micropatterning of
43
44 a Superhydrophobic Surface: Toward Biomimetic Fog Harvesting Surfaces. *J. Mater. Chem. A*
45
46 **2015**, *3* (6), 2844–2852. <https://doi.org/10.1039/c4ta05862c>.
47
48
49
50 (6) Sakurada, S.; Sole-Gras, M.; Christensen, K.; Wallace, D. B.; Huang, Y. Liquid-Absorbing System-
51
52 Assisted Intersecting Jets Printing of Soft Structures from Reactive Biomaterials. *Addit. Manuf.*
53
54 **2020**, *31*. <https://doi.org/10.1016/j.addma.2019.100934>.
55
56
57

- 1
2 (7) Boland, T.; Xu, T.; Damon, B.; Cui, X. Application of Inkjet Printing to Tissue Engineering.
3
4 *Biotechnology Journal*. September 2006, pp 910–917. <https://doi.org/10.1002/biot.200600081>.
5
6
7
8 (8) Wu, L.; Dong, Z.; Kuang, M.; Li, Y.; Li, F.; Jiang, L.; Song, Y. Printing Patterned Fine 3D Structures
9
10 by Manipulating the Three Phase Contact Line. *Adv. Funct. Mater.* **2015**, *25* (15), 2237–2242.
11
12 <https://doi.org/10.1002/adfm.201404559>.
13
14
15
16 (9) Boukhalfa, H. H.; Massinon, M.; Belhamra, M.; Lebeau, F. Contribution of Spray Droplet Pinning
17
18 Fragmentation to Canopy Retention. *Crop Prot.* **2014**, *56*, 91–97.
19
20 <https://doi.org/10.1016/j.cropro.2013.11.018>.
21
22
23
24 (10) Zheng, L.; Cao, C.; Cao, L.; Chen, Z.; Huang, Q.; Song, B. Bounce Behavior and Regulation of
25
26 Pesticide Solution Droplets on Rice Leaf Surfaces. *J. Agric. Food Chem.* **2018**, *66* (44), 11560–
27
28 11568. <https://doi.org/10.1021/acs.jafc.8b02619>.
29
30
31
32 (11) Breitenbach, J.; Roisman, I. V.; Tropea, C. From Drop Impact Physics to Spray Cooling Models: A
33
34 Critical Review. *Exp. Fluids* **2018**, *59* (3), 55. <https://doi.org/10.1007/s00348-018-2514-3>.
35
36
37
38 (12) Bjørge, J. S.; Bjørkheim, S. A.; Metallinou, M. M.; Log, T.; Frette, Ø. Influence of Acetone and
39
40 Sodium Chloride Additives on Cooling Efficiency of Water Droplets Impinging onto Hot Metal
41
42 Surfaces. *Energies* **2019**, *12* (12), 2358. <https://doi.org/10.3390/en12122358>.
43
44
45
46 (13) Yang, Q.; Luo, Z.; Jiang, F.; Luo, Y.; Tan, S.; Lu, Z.; Zhang, Z.; Liu, W. Air Cushion Convection
47
48 Inhibiting Icing of Self-Cleaning Surfaces. *ACS Appl. Mater. Interfaces* **2016**, *8* (42), 29169–29178.
49
50 <https://doi.org/10.1021/acsami.6b10165>.
51
52
53
54 (14) Blossey, R. Self-Cleaning Surfaces - Virtual Realities. *Nat. Mater.* **2003**, *2* (5), 301–306.
55
56 <https://doi.org/10.1038/nmat856>.
57
58

- 1
2 (15) Wisdom, K. M.; Watson, J. A.; Qu, X.; Liu, F.; Watson, G. S.; Chen, C. H. Self-Cleaning of
3 Superhydrophobic Surfaces by Self-Propelled Jumping Condensate. *Proc. Natl. Acad. Sci. U. S. A.*
4
5
6
7 **2013**, *110* (20), 7992–7997. <https://doi.org/10.1073/pnas.1210770110>.
8
9
- 10 (16) Wang, N.; Xiong, D.; Deng, Y.; Shi, Y.; Wang, K. Mechanically Robust Superhydrophobic Steel
11 Surface with Anti-Icing, UV-Durability, and Corrosion Resistance Properties. *ACS Appl. Mater.*
12
13
14
15 *Interfaces* **2015**, *7* (11), 6260–6272. <https://doi.org/10.1021/acsami.5b00558>.
16
17
- 18 (17) Mohamed, A. M. A.; Abdullah, A. M.; Younan, N. A. Corrosion Behavior of Superhydrophobic
19 Surfaces: A Review. *Arabian Journal of Chemistry*. Elsevier 2015, pp 749–765.
20
21
22
23 <https://doi.org/10.1016/j.arabjc.2014.03.006>.
24
25
- 26 (18) Chen, Y.; Chen, S.; Yu, F.; Sun, W.; Zhu, H.; Yin, Y. Fabrication and Anti-Corrosion Property of
27 Superhydrophobic Hybrid Film on Copper Surface and Its Formation Mechanism. *Surf. Interface*
28
29
30
31 *Anal.* **2009**, *41* (11), 872–877. <https://doi.org/10.1002/sia.3102>.
32
33
- 34 (19) Solomatin, Y.; Shlegel, N. E.; Strizhak, P. A. Atomization of Promising Multicomponent Fuel
35 Droplets by Their Collisions. *Fuel* **2019**, *255*. <https://doi.org/10.1016/j.fuel.2019.115751>.
36
37
38
39
- 40 (20) Tang, C.; Qin, M.; Weng, X.; Zhang, X.; Zhang, P.; Li, J.; Huang, Z. Dynamics of Droplet Impact on
41 Solid Surface with Different Roughness. *Int. J. Multiph. Flow* **2017**, *96*, 56–69.
42
43
44
45 <https://doi.org/10.1016/j.ijmultiphaseflow.2017.07.002>.
46
47
- 48 (21) Kavale, M. S.; Mahadik, D. B.; Parale, V. G.; Wagh, P. B.; Gupta, S. C.; Rao, A. V.; Barshilia, H. C.
49 Optically Transparent, Superhydrophobic Methyltrimethoxysilane Based Silica Coatings without
50
51
52
53 Silylating Reagent. *Appl. Surf. Sci.* **2011**, *258* (1), 158–162.
54
55
56 <https://doi.org/10.1016/j.apsusc.2011.08.023>.
57
58
59
60

- 1
2 (22) Barati Darband, G.; Aliofkhazraei, M.; Khorsand, S.; Sokhanvar, S.; Kaboli, A. Science and
3
4 Engineering of Superhydrophobic Surfaces: Review of Corrosion Resistance, Chemical and
5
6 Mechanical Stability. *Arab. J. Chem.* **2020**, *13* (1), 1763–1802.
7
8 <https://doi.org/10.1016/j.arabjc.2018.01.013>.
9
10
11
12 (23) Bai, H.; Wang, L.; Ju, J.; Sun, R.; Zheng, Y.; Jiang, L. Efficient Water Collection on Integrative
13
14 Bioinspired Surfaces with Star-Shaped Wettability Patterns. *Adv. Mater.* **2014**, *26* (29), 5025–
15
16 5030. <https://doi.org/10.1002/adma.201400262>.
17
18
19
20 (24) Li, J.; Song, Y.; Zheng, H.; Feng, S.; Xu, W.; Wang, Z. Designing Biomimetic Liquid Diodes. *Soft*
21
22 *Matter* **2019**, *15* (9), 1902–1915. <https://doi.org/10.1039/c9sm00072k>.
23
24
25
26 (25) Regulagadda, K.; Bakshi, S.; Das, S. K. Droplet Ski-Jumping on an Inclined Macro-Textured
27
28 Superhydrophobic Surface. *Appl. Phys. Lett.* **2018**, *113* (10), 103702.
29
30 <https://doi.org/10.1063/1.5048301>.
31
32
33
34 (26) Mouterde, T.; Lehoucq, G.; Xavier, S.; Checco, A.; Black, C. T.; Rahman, A.; Midavaine, T.; Clanet,
35
36 C.; Quéré, D. Antifogging Abilities of Model Nanotextures. *Nat. Mater.* **2017**, *16* (6), 658–663.
37
38 <https://doi.org/10.1038/nmat4868>.
39
40
41
42 (27) Rioboo, R.; Tropea, C.; Marengo, M. Outcomes from a Drop Impact on Solid Surfaces. *At. Sprays*
43
44 **2001**, *11* (2), 155–165. <https://doi.org/10.1615/AtomizSpr.v11.i2.40>.
45
46
47
48 (28) Ma, H.; Liu, C.; Li, X.; Huang, H.; Dong, J. Deformation Characteristics and Energy Conversion
49
50 during Droplet Impact on a Water Surface. *Phys. Fluids* **2019**, *31* (6).
51
52 <https://doi.org/10.1063/1.5099228>.
53
54
55
56 (29) Chen, B.; Wang, B.; Mao, F.; Wen, J.; Tian, R.; Lu, C. Experimental Study of Droplet Impacting on
57
58
59
60

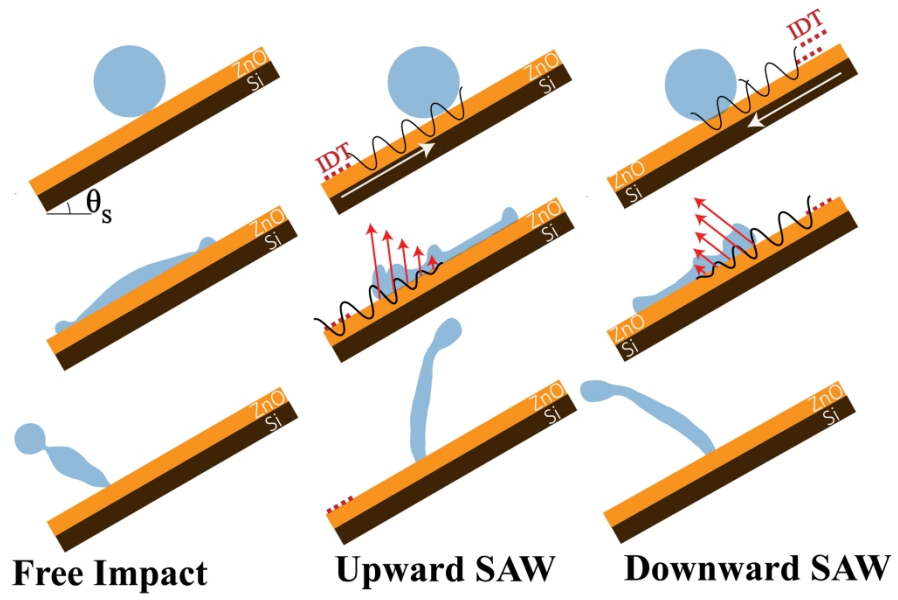
- 1
2 Inclined Wetted Wall in Corrugated Plate Separator. *Ann. Nucl. Energy* **2020**, *137*.
3
4 <https://doi.org/10.1016/j.anucene.2019.107155>.
5
6
7
8 (30) Bayer, I. S.; Megaridis, C. M. Contact Angle Dynamics in Droplets Impacting on Flat Surfaces with
9
10 Different Wetting Characteristics. *J. Fluid Mech.* **2006**, *558*, 415–449.
11
12 <https://doi.org/10.1017/S0022112006000231>.
13
14
15
16 (31) Šikalo, Š.; Tropea, C.; Ganić, E. N. Impact of Droplets onto Inclined Surfaces. *J. Colloid Interface*
17
18 *Sci.* **2005**, *286* (2), 661–669. <https://doi.org/10.1016/j.jcis.2005.01.050>.
19
20
21
22 (32) Bird, J. C.; Tsai, S. S. H.; Stone, H. A. Inclined to Splash: Triggering and Inhibiting a Splash with
23
24 Tangential Velocity. *New J. Phys.* **2009**, *11* (6), 063017. [https://doi.org/10.1088/1367-](https://doi.org/10.1088/1367-2630/11/6/063017)
25
26 [2630/11/6/063017](https://doi.org/10.1088/1367-2630/11/6/063017).
27
28
29
30 (33) Chiarot, P. R.; Jones, T. B. Grazing Impact of Continuous Droplet Streams with a
31
32 Superhydrophobic Surface. *Exp. Fluids* **2010**, *49* (5), 1109–1119.
33
34 <https://doi.org/10.1007/s00348-010-0860-x>.
35
36
37
38 (34) Zheng, L.; Li, Z.; Bourdo, S.; Khedir, K. R.; Asar, M. P.; Ryerson, C. C.; Biris, A. S. Exceptional
39
40 Superhydrophobicity and Low Velocity Impact Icephobicity of Acetone-Functionalized Carbon
41
42 Nanotube Films. *Langmuir* **2011**, *27* (16), 9936–9943. <https://doi.org/10.1021/la201548k>.
43
44
45
46 (35) Hao, J.; Lu, J.; Lee, L.; Wu, Z.; Hu, G.; Floryan, J. M. Droplet Splashing on an Inclined Surface. *Phys.*
47
48 *Rev. Lett.* **2019**, *122* (5). <https://doi.org/10.1103/PhysRevLett.122.054501>.
49
50
51
52 (36) Yeong, Y. H.; Burton, J.; Loth, E.; Bayer, I. S. Drop Impact and Rebound Dynamics on an Inclined
53
54 Superhydrophobic Surface. *Langmuir* **2014**, *30* (40), 12027–12038.
55
56 <https://doi.org/10.1021/la502500z>.
57
58

- 1
2 (37) Antonini, C.; Villa, F.; Marengo, M. Oblique Impacts of Water Drops onto Hydrophobic and
3 Superhydrophobic Surfaces: Outcomes, Timing, and Rebound Maps. *Exp. Fluids* **2014**, *55* (4).
4 <https://doi.org/10.1007/s00348-014-1713-9>.
5
6
7
8
9
10 (38) LeClear, S.; LeClear, J.; Abhijeet; Park, K. C.; Choi, W. Drop Impact on Inclined Superhydrophobic
11 Surfaces. *J. Colloid Interface Sci.* **2016**, *461*, 114–121. <https://doi.org/10.1016/j.jcis.2015.09.026>.
12
13
14
15 (39) Wang, H.; Liu, C.; Zhan, H.; Liu, Y. Droplet Asymmetric Bouncing on Inclined Superhydrophobic
16 Surfaces. *ACS Omega* **2019**, *4* (7), 12238–12243. <https://doi.org/10.1021/acsomega.9b01348>.
17
18
19
20
21 (40) De Ruiter, J.; Soto, D.; Varanasi, K. K. Self-Peeling of Impacting Droplets. *Nat. Phys.* **2018**, *14* (1),
22 35–39. <https://doi.org/10.1038/NPHYS4252>.
23
24
25
26
27 (41) Damak, M.; Mahmoudi, S. R.; Hyder, M. N.; Varanasi, K. K. Enhancing Droplet Deposition through
28 In-Situ Precipitation. *Nat. Commun.* **2016**, *7*. <https://doi.org/10.1038/ncomms12560>.
29
30
31
32
33 (42) Hao, C.; Li, J.; Liu, Y.; Zhou, X.; Liu, Y.; Liu, R.; Che, L.; Zhou, W.; Sun, D.; Li, L.; Xu, L.; Wang, Z.
34 Superhydrophobic-like Tunable Droplet Bouncing on Slippery Liquid Interfaces. *Nat. Commun.*
35 **2015**, *6*. <https://doi.org/10.1038/ncomms8986>.
36
37
38
39
40
41 (43) Zhang, R.; Hao, P.; He, F. Drop Impact on Oblique Superhydrophobic Surfaces with Two-Tier
42 Roughness. *Langmuir* **2017**, *33* (14), 3556–3567.
43 <https://doi.org/10.1021/acs.langmuir.7b00569>.
44
45
46
47
48
49 (44) Fu, Y. Q.; Luo, J. K.; Nguyen, N. T.; Walton, A. J.; Flewitt, A. J.; Zu, X. T.; Li, Y.; McHale, G.;
50 Matthews, A.; Iborra, E.; Du, H.; Milne, W. I. Advances in Piezoelectric Thin Films for Acoustic
51 Biosensors, Acoustofluidics and Lab-on-Chip Applications. *Prog. Mater. Sci.* **2017**, *89*, 31–91.
52 <https://doi.org/10.1016/j.pmatsci.2017.04.006>.
53
54
55
56
57
58
59
60

- 1
2 (45) Guo, Y. J.; Dennison, A. P.; Li, Y.; Luo, J.; Zu, X. T.; Mackay, C. L.; Langridge-Smith, P.; Walton, A.
3
4 J.; Fu, Y. Q. Nebulization of Water/Glycerol Droplets Generated by ZnO/Si Surface Acoustic Wave
5
6 Devices. *Microfluid. Nanofluidics* **2015**, *19* (2), 273–282. [https://doi.org/10.1007/s10404-014-](https://doi.org/10.1007/s10404-014-1501-0)
7
8 1501-0.
9
10
11
12 (46) Bui, T. H.; Nguyen, V.; Vollebregt, S.; Morana, B.; van Zeijl, H.; Chu Duc, T.; Sarro, P. M. Effect of
13
14 Droplet Shrinking on Surface Acoustic Wave Response in Microfluidic Applications. *Appl. Surf.*
15
16 *Sci.* **2017**, *426*, 253–261. <https://doi.org/10.1016/j.apsusc.2017.07.140>.
17
18
19
20
21 (47) Barani, A.; Paktinat, H.; Janmaleki, M.; Mohammadi, A.; Mosaddegh, P.; Fadaei-Tehrani, A.;
22
23 Sanati-Nezhad, A. Microfluidic Integrated Acoustic Waving for Manipulation of Cells and
24
25 Molecules. *Biosens. Bioelectron.* **2016**, *85*, 714–725.
26
27 <https://doi.org/10.1016/j.bios.2016.05.059>.
28
29
30
31 (48) Yeo, L. Y.; Chang, H. C.; Chan, P. P. Y.; Friend, J. R. Microfluidic Devices for Bioapplications. *Small*
32
33 **2011**, *7* (1), 12–48. <https://doi.org/10.1002/smll.201000946>.
34
35
36
37 (49) Biroun, M. H.; Rahmati, M. T.; Jangi, M.; Tao, R.; Chen, B. X.; Fu, Y. Q. Computational and
38
39 Experimental Analysis of Droplet Transportation/Jetting Behaviours Driven by Thin Film Surface
40
41 Acoustic Waves. *Sensors Actuators, A Phys.* **2019**, *299*, 111624.
42
43 <https://doi.org/10.1016/j.sna.2019.111624>.
44
45
46
47 (50) Shiokawa, S.; Matsui, Y.; Ueda, T. Study on Saw Streaming and Its Application to Fluid Devices.
48
49 *Jpn. J. Appl. Phys.* **1990**, *29* (S1), 137–139. <https://doi.org/10.7567/JJAPS.29S1.137>.
50
51
52
53 (51) Ding, X.; Li, P.; Lin, S. C. S.; Stratton, Z. S.; Nama, N.; Guo, F.; Slotcavage, D.; Mao, X.; Shi, J.;
54
55 Costanzo, F.; Huang, T. J. Surface Acoustic Wave Microfluidics. *Lab Chip* **2013**, *13* (18), 3626–
56
57
58
59
60

- 1
2 3649. <https://doi.org/10.1039/c3lc50361e>.
3
4
- 5 (52) Alghane, M.; Fu, Y. Q.; Chen, B. X.; Li, Y.; Desmulliez, M. P. Y.; Walton, A. J. Streaming Phenomena
6 in Microdroplets Induced by Rayleigh Surface Acoustic Wave. *J. Appl. Phys.* **2011**, *109* (11).
7
8 <https://doi.org/10.1063/1.3586040>.
9
10
11
12
- 13 (53) Mehdi H. Biroun, Jie Li, Ran Tao, Mohammad Rahmati, Glen McHale, Linxi Dong, Mehdi Jangi,
14 Hamdi Torun, Y. F. Acoustic Waves for Active Reduction of Droplet Impact Contact Time. *Phys.*
15
16 *Rev. Appl.* **2020**, No. (Accepted Manuscript).
17
18
19
20
- 21 (54) Sankaranarayanan, S. K. R. S.; Cular, S.; Bhethanabotla, V. R.; Joseph, B. Flow Induced by Acoustic
22 Streaming on Surface-Acoustic-Wave Devices and Its Application in Biofouling Removal: A
23
24 Computational Study and Comparisons to Experiment. *Phys. Rev. E - Stat. Nonlinear, Soft Matter*
25
26 *Phys.* **2008**, *77* (6), 1–19. <https://doi.org/10.1103/PhysRevE.77.066308>.
27
28
29
30
- 31 (55) Tao, R.; Mchale, G.; Reboud, J.; Cooper, J. M.; Torun, H.; Luo, J. T.; Luo, J.; Yang, X.; Zhou, J.;
32
33 Canyelles-Pericas, P.; Wu, Q.; Fu, Y. Hierarchical Nanotexturing Enables Acoustofluidics on
34
35 Slippery yet Sticky, Flexible Surfaces. *Nano Lett.* **2020**, *20* (5), 3263–3270.
36
37 <https://doi.org/10.1021/acs.nanolett.0c00005>.
38
39
40
41
- 42 (56) Shirtcliffe, N. J.; McHale, G.; Atherton, S.; Newton, M. I. An Introduction to Superhydrophobicity.
43
44 *Advances in Colloid and Interface Science*. Elsevier December 15, 2010, pp 124–138.
45
46 <https://doi.org/10.1016/j.cis.2009.11.001>.
47
48
49
- 50 (57) Ahmed, G.; Sellier, M.; Jermy, M.; Taylor, M. Modeling the Effects of Contact Angle Hysteresis
51
52 on the Sliding of Droplets down Inclined Surfaces. *Eur. J. Mech. B/Fluids* **2014**, *48*, 218–230.
53
54 <https://doi.org/10.1016/j.euromechflu.2014.06.003>.
55
56
57
58

- 1
2 (58) Aminzadeh, M.; Maleki, A.; Firoozabadi, B.; Afshin, H. On the Motion of Newtonian and Non-
3
4 Newtonian Liquid Drops. *Sci. Iran.* **2012**, *19* (5), 1265–1278.
5
6 <https://doi.org/10.1016/j.scient.2011.09.022>.
7
8
9
10 (59) Tian, J. M.; Chen, B. Dynamic Behavior of Non-Evaporative Droplet Impact on a Solid Surface:
11
12 Comparative Study of R113, Water, Ethanol and Acetone. *Exp. Therm. Fluid Sci.* **2019**, *105*, 153–
13
14 164. <https://doi.org/10.1016/j.expthermflusci.2019.03.024>.
15
16
17
18 (60) Bisighini, A.; Cossali, G. E.; Tropea, C.; Roisman, I. V. Crater Evolution after the Impact of a Drop
19
20 onto a Semi-Infinite Liquid Target. *Phys. Rev. E - Stat. Nonlinear, Soft Matter Phys.* **2010**, *82* (3),
21
22 036319. <https://doi.org/10.1103/PhysRevE.82.036319>.
23
24
25
26 (61) Lee, J. B.; Derome, D.; Dolatabadi, A.; Carmeliet, J. Energy Budget of Liquid Drop Impact at
27
28 Maximum Spreading: Numerical Simulations and Experiments. *Langmuir* **2016**, *32*, 10.
29
30 <https://doi.org/10.1021/acs.langmuir.5b03848>.
31
32
33
34
35
36
37
38
39
40
41
42
43
44
45
46
47
48
49
50
51
52
53
54
55
56
57
58
59
60



564x373mm (150 x 150 DPI)